Modelling the vortex induced vibrations of sea fastened wind turbine towers using a wake oscillator

Timothy Jessurun

MSc. Thesis

Modelling the vortex induced vibrations of sea fastened wind turbine towers using a wake oscillator

MSc Thesis

By

T.D. Jessurun

in partial fulfilment of the requirements for the degree of

Master of Science
in Offshore and Dredging Engineering

at the Delft University of Technology,
to be defended on Wednesday March 27, 2019 at 2:00 PM.

Thesis committee:	Prof. dr. A. V. Metrikine,	TU Delft
	Dr.Ir. K.N. van Dalen,	TU Delft
	MSc. Y. Qu,	TU Delft
	Ing. M. Kroon,	Seafox

This page is intentionally left blank

Preface

I would like to express a word of gratitude towards all the people who have helped and supported me throughout the writing of my thesis and finishing of my study here in Delft. This was an unforgettable journey which I could not have finished alone. A special thanks to:

My supervisor at the university, Yang Qu for his daily supervision and guidance. Professor Andrei Metrikine for his critical feedback and guidance.

My supervisor at Seafox, Martijn Kroon who provided me with the practical information. Further I would like to thank the kind colleagues at Seafox. With whom I had a very good time.

My family, for their unconditional support.

Last but not least my girlfriend, Nicole for her patience, encouragement and support.

T.D. Jessurun

Delft, March 27 2019

This page is intentionally left blank

Abstract

It is well known that for tall cylindrical structures under wind action, such as wind turbine towers, vortex induced vibrations (VIV) may occur. During the installation of offshore wind turbine towers there are different stages of transport where we might deal with VIV.

The main objective of this thesis is to explore the possibility of modeling the VIV of flexible cylindrical structures by means of an existing wake oscillator model. Sub objectives are to investigate the influence of the deck stiffness and vessel motions on the VIV. And also, the effectiveness of strakes as mitigation for VIV is investigated.

From the literature study it is found that an existing wake-oscillator model with acceleration coupling is a good way to model the VIV of a rigid cylinder that is free to vibrate in water. This wake oscillator model, which was tuned to the experiments in water, is then tuned to an experiment where the rigid cylinder was free to vibrate in air. These free vibration experiments were all done in the sub critical flow regime.

In the next step the model is extended to model the VIV of flexible cylindrical structures. In an attempt to validate, this model is used to simulate the cross-flow amplitude of a in situ chimney on whom measurements were done during VIV. Due to the size of the in situ chimney, the Reynolds number at which VIV occurred suggests that we are in the super critical flow regime. However, the measured Strouhal number had a frequent value of 0.21 which is common for the sub critical flow regime. From the simulations it was found that by making use of the force coefficients from the super critical regime good agreement is found between the simulated and measured crossflow amplitude, while adopting force coefficients from the sub critical regime, the model significantly over predicted the response.

Finally, the model is applied in a case study with a wind turbine tower. A total of four cases are investigated. From this case study it was found that a stiff deck will result in VIV at higher windspeeds, but will also increase the loads. The VIV of the tower is hardly influenced by the vessel motion since the frequencies of the two are far apart. According to the model, covering the top one third of the tower with strakes significantly reduce the VIV, but with a penalty of increased in-line bending load on the deck.

This page is intentionally left blank

Nomenclature

D_o	Outer diameter	$[m]$
V_n	Reduced velocity	$[-]$
a_1	Proportional damping coefficient	$[-]$
f_n	Natural frequency	$[1/s]$
f_s	Vortex shedding frequency	$[1/s]$
k_r	Rotational stiffness	$[Nm/rad]$
m^*	Mass ratio	$[-]$
δ	Logarithmic decrement	$[-]$
ω_f	Forcing frequency	$[1/s]$
ω_s	Vortex shedding frequency	$[1/s]$
A_f	Forcing amplitude	$[-]$
A	Tuning parameter	$[-]$
D	Diameter	$[m]$
E	Youngs modulus	$[N/m^2]$
C_{LO}	Stationary lift force coefficient cylinder	$[-]$
C_{D0}	Stationary drag force coefficient cylinder	$[-]$
P	Compression	$[N]$
Re	Reynolds number	$[-]$
St	Strouhal number	$[-]$
m	Mass	$[kg]$
q	Wake parameter	$[-]$
v	Undisturbed flow velocity	$[m/s]$
α	Power law exponent for wind	$[-]$
ζ	Damping ratio	$[-]$
ν	Kinematic viscosity	$[m^2/s]$
ρ	Density	$[kg/m^3]$
ϵ	tuning parameter	[-]

This page is intentionally left blank

Table of Contents

1 Introduction

1.1 General information

There is an increasing demand for renewable energy. In the transition to renewables, wind energy plays a major role. To sustain the demand, offshore wind farms are increasing in capacity and thus are also their tower structures.

Seafox is an offshore contractor specialized in jack-up structures. A jack-up structure is a 'ship' that is able to elevate itself above sea level. This has many advantages, for example it makes it possible to do installation procedures at sea without the effect of ship motions.

With one of their vessels, the 'Seafox 5', Seafox is going to install wind turbines. Such an installation project consists of different stages of transport. First the vessel is in the harbor where the towers are loaded and sea fastened on the deck. Subsequent next stages of transport are sailing to location and then installation at location. In the event of a storm the vessel is jacked up.

Figure 1-1 Seafox 5 in the harbour with the wind turbines towers on quayside to be loaded

Problem statement:

It is well known that for cylindrical structures, such as chimneys, marine pipelines or even a wind turbine tower in a fluid flow, vortex induced vibrations (VIV) may occur. These vibrations can lead to high dynamic loads or a collision of the transferring towers. This may affect the fatigue life of the sea fastening or even the deck of the vessel. According to Seafox, the effects of the VIV are normally considered small. However, wind turbines are recently increasing in size. This means that taller towers are being transported, and these taller structures may be more sensitive to VIV.

For an upcoming wind farm project Seafox B.V. needs to transport these large towers, which have already reached up to a height of 80 m and a diameter of 6m. For this reason, fundamental research and insight is required on the VIV effects of these large wind turbine towers.

1.2 Scope of the thesis

Research objectives:

The main goal of this research is to explore the possibility of modelling the VIV of flexible cylindrical structures by means of an existing wake oscillator model.

The sub objectives in this research are to investigate the influence of the deck stiffness and the vessel motions on the VIV. Also, the effectiveness of strakes as mitigation for VIV is investigated.

Problem Approach:

The approach that is taken, is to first get an understanding of the mechanism of VIV. For this a literature study is done. Here the importance of the Reynolds number range is emphasized. Also, the understanding of the difference found between VIV experiments in water (low mass damping) and VIV experiments in air (high mass damping) is gained here.

From the literature study it is found that an existing wake-oscillator model with acceleration coupling is a good way to model the VIV of a rigid cylinder that was free to vibrate in water. This existing wake-oscillator model, which was tuned to the experiments in water, is then tuned to an experiment where the rigid cylinder was free to vibrate in air. It is important to note that all these experiments were done in the subcritical flow regime.

In the next step an attempt is made to extend the model to model the VIV of flexible cylindrical structures. For validation purposes the model is used to predict the crossflow amplitude of an in-situ chimney under VIV loads on whom measurements where done. Finally, the model is applied in a case study. Here different cases are investigated for a wind turbine tower under VIV loading.

1.3 Thesis outline

Chapter 1:	In this chapter a general introduction is given to the problem, together with the research objectives and the problem approach.
Chapter 2:	Here general understanding of the problem is obtained, and the mechanism behind vortex shedding and VIV is studied. Some suppression measures against VIV are discussed and finally the wind velocity profile is explained.
Chapter 3:	This chapter explains the modelling of a rigid cylinder vibrating under vortex induced vibrations.
Chapter 4:	Following up on the previous chapter the extension is made to model flexible cylinders under vortex induced vibrations.
Chapter 5:	In this chapter several case studies for different stages of transport are investigated.
Chapter 6:	Based on the knowledge gained in the previous chapters conclusions are drawn and recommendations are given.

2 Literature study

In this chapter, an introduction to the technical background and knowledge around vortex shedding is given. First the vortex shedding process for a stationary cylinder is explained. After which different flow regimes are distinguished based on the Reynolds number. In the second part of this chapter a look will be taken into rigid cylinders that are free to vibrate, resulting in vortex induced vibrations (VIV). Then, a short overview is given on different ways to model VIV. Finally, the wind velocity profile that is used in this thesis is explained.

2.1 Vortex shedding on a stationary cylinder

2.1.1 Vortex shedding mechanism

Submerging a solid body in a uniform fluid flow results in a disturbed and unstable flow field. This disturbance gives rise to vortices being shed in the wake. The vortex shedding mechanism is illustrated in figure 2.1. As a current flows along a cylinder, vortex A evolves in size and pulls vortex B in the wake of the body causing an interaction between both vortices; Figure 2-1 (a); Due to the opposite signs of vortex A and B, the vorticity supply to vortex A is interrupted. At this moment vortex A releases the cylinder and vortex B will take the role of vortex A as shown in Figure 2-1b. This shedding process is repeated in time on opposite sides of the cylinder and is known as “alternate vortex shedding”.

(a) (b)

Figure 2-1 Vortex shedding mechanism. (Sumer & Fredsøe, 1997)

2.1.2 Reynolds number

The Reynolds number (Re) is used to describe and classify dynamic flows. The equation for the Reynolds number is given by:

$$Re = \frac{D \cdot V}{\nu} \qquad (2.1)$$

Where:

Re = Reynolds number [-]
D = Cylinder diameter [m]
V = Flow velocity [ms-1]
ν = Kinematic viscosity [m^{2}s^{-1}]

Depending on the Reynolds number different flow regimes can be distinguished. An overview of the different flow regimes can be found in Figure 2-2. For small values of Re (Re<5) no separation of the boundary layer occurs. From Reynolds numbers as low as 40 and up till 200, the wake becomes unstable and vortices shed alternately at either side of the cylinder result in a laminar vortex street.

In this region, the shedding does not vary in the span wise direction and is therefore two dimensional. The shedding becomes three dimensional at Re number of 400. In that event the vortices are shed in cells in the span wise direction. Furthermore, Reynolds numbers between 200 and 300 result a transition from laminar to turbulent in the wake. From 300<Re< 3.10^5 the wake is completely turbulent, this is known as the subcritical region. An increase in Reynolds number up to $3.5.10^5$ results in a one-sided turbulent boundary layer at the separation point. This region is also recognised as the critical flow region. The next region, the supercritical flow region, is differentiated by turbulent boundary layers separation on both sides of the cylinders. In the upper region of Reynolds numbers Re> 4.10^6, the boundary layer over the cylinder is completely turbulent.

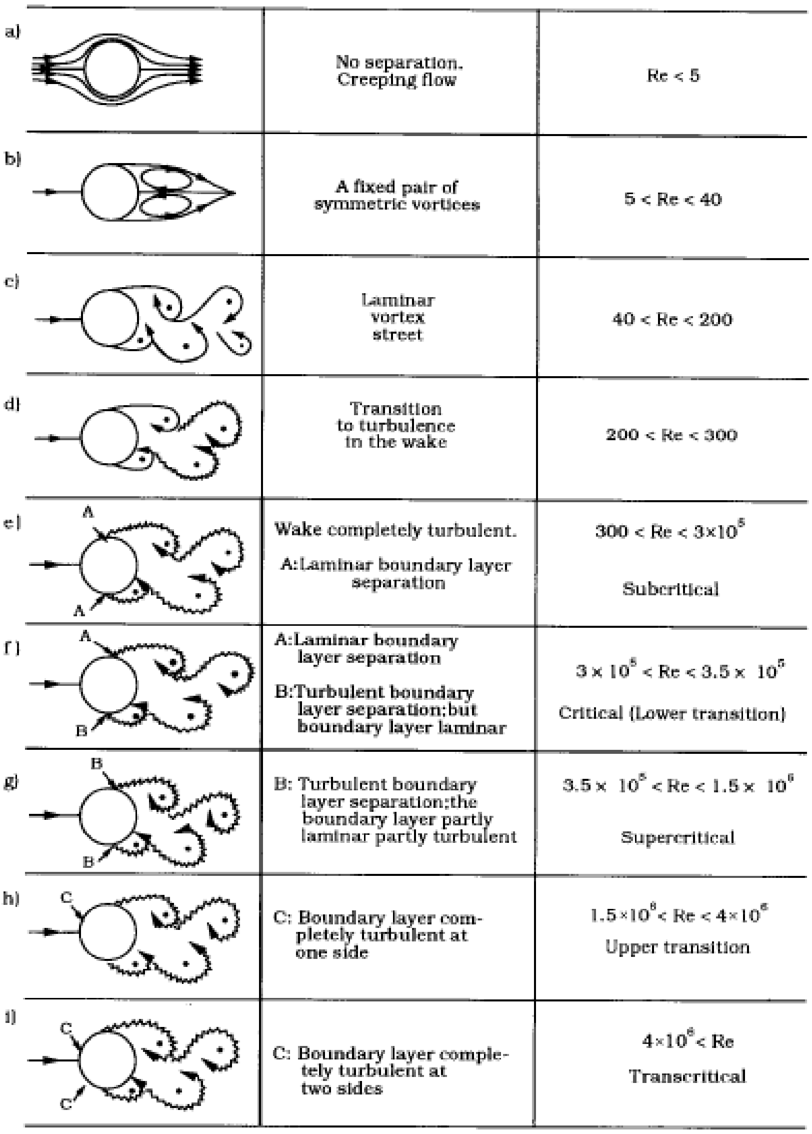

a)	No separation. Creeping flow	Re < 5
b)	A fixed pair of symmetric vortices	5 < Re < 40
c)	Laminar vortex street	40 < Re < 200
d)	Transition to turbulence in the wake	200 < Re < 300
e)	Wake completely turbulent. A:Laminar boundary layer separation	300 < Re < 3×10^5 Subcritical
f)	A:Laminar boundary layer separation B:Turbulent boundary layer separation;but boundary layer laminar	3×10^5 < Re < 3.5×10^5 Critical (Lower transition)
g)	B: Turbulent boundary layer separation;the boundary layer partly laminar partly turbulent	3.5×10^5 < Re < 1.5×10^6 Supercritical
h)	C: Boundary layer completely turbulent at one side	1.5×10^6 < Re < 4×10^6 Upper transition
i)	C: Boundary layer completely turbulent at two sides	4×10^6 < Re Transcritical

Figure 2-2 Regimes of fluid flow across a smooth circular cylinder. (Sumer & Fredsøe, 1997)

It is interesting to notice that given the large diameters of the towers, the Reynolds numbers that we deal with are expected to be outside the subcritical rage. The typical values of the Reynolds number for the towers are shown in Table 2-1, with different colours to indicate the flow regimes. These are as follows:

Yellow:	Indicates the subcritical range, this is only the case for very small windspeeds
Red:	Indicates the critical/supercritical range, this is highly likely for operational windspeeds
Green:	Indicates the trans critical range, this is highly likely for storm conditions.

Table 2-1 Reynolds number for typical tower dimensions and windspeeds. Assumed v = 1.51E-05

Diameter [m]	**Wind speed [m/s]**							
	1	**5**	**10**	**15**	**20**	**25**	**30**	**35**
4	2.6E+05	1.3E+06	2.6E+06	4.0E+06	5.3E+06	6.6E+06	7.9E+06	9.3E+06
5	3.3E+05	1.7E+06	3.3E+06	5.0E+06	6.6E+06	8.3E+06	9.9E+06	1.2E+07
6	4.0E+05	2.0E+06	4.0E+06	6.0E+06	7.9E+06	9.9E+06	1.2E+07	1.4E+07

2.1.3 Pressure field and fluid forces

Due to the fluctuations in flow speed around the cylinder a pressure field as shown in Figure 2-3 is formed. Integration of this pressures over the cylinders periphery results in the total fluid force on the cylinder. This fluid force can thus be decomposed in an in-line component and a cross-flow component. Aside from these components the fluid force also consists of a shear force as a result of friction. However, this force is not considered due to its insignificant magnitude. The inline component is the drag force and the cross-flow component is the lift force for stationary cylinders. The forces acting on the cylinder are oscillating as a result of alternated shedding of the vortices.

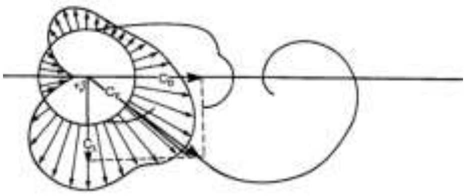

Figure 2-3. Pressure field and wake forms at Re = 112 000. [2]

In Figure 2-4 the relation between the mean drag coefficient as a function of the Reynolds number for a stationary cylinder is shown. It can be noted that in the subcritical region the stationary drag coefficient has a constant value of approximately $C_{D0} = 1.2$. Furthermore, in the regimes after the critical range the values decrease at once. The same behaviour is observed for the Root Mean Square value (RMS) of the stationary lift force coefficient, C_{L0}. In the subcritical range it is common to use $C_{L0} = 0.3$.

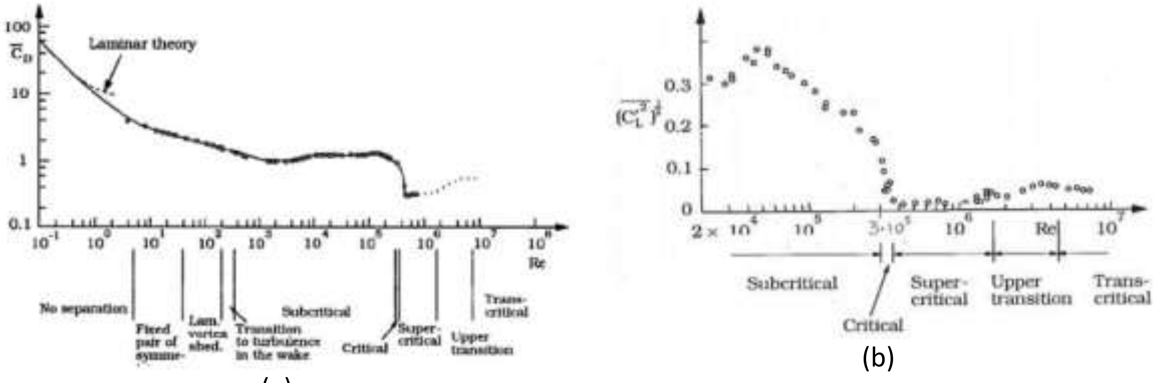

(a)

(b)

Figure 2-4 Force coefficients as a function of the Reynolds number. (a) Drag coefficient; (b) Lift coefficient

2.1.4 Strouhal number

The Strouhal number is another important parameter describing the flow. For a stationary cylinder, the vortex shedding frequency follows the Strouhal relation given by equation (2.2).

$$St = \frac{f_s \cdot D}{V} \tag{2.2}$$

Where:

St	=	Strouhal number	[-]
f_s	=	Vortex shedding frequency	[s^{-1}]
D	=	Diameter	[m]
V	=	Velocity	[ms^{-1}]

For a smooth cylinder, Figure 2-5 shows how the Strouhal number changes for different flow regimes classified by Reynolds number. Initiating in the laminar flow regime at a Strouhal number of 0.1, it reaches a value of 0.2 in the Reynolds number regime of transition to turbulence in the wake. With a gradually increasing Reynolds number up to the critical transition, the Strouhal number stays steady around 0.2 till the critical transition region. After which, the Strouhal number swiftly increases and subsequently decreases once more when in the super critical region.

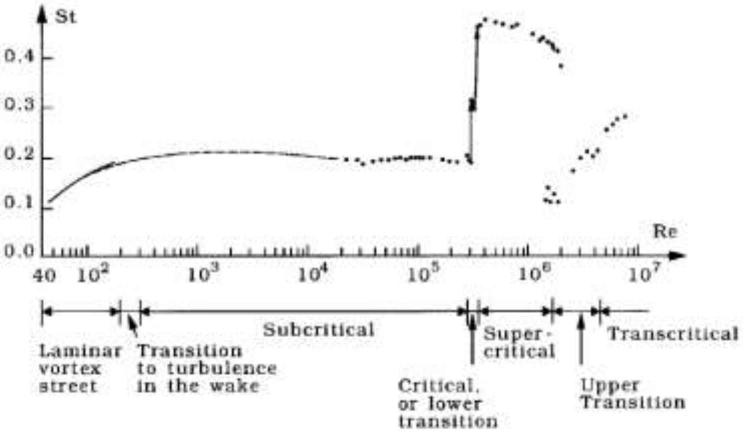

Figure 2-5: Strouhal number for a smooth cylinder as a function of the Reynolds number. (Sumer & Fredsøe, 1997)

2.2 Vortex shedding from an oscillating cylinder

Numerous experimental studies have been done on the behavior of cylinders under vortex excitation. Generally speaking, there are two types of experiments that can be done in studying VIV. There are free vibration experiments. Here usually a spring mounted cylinder is subject to an increasing or decreasing current flow in a wind tunnel or water channel. The vibration amplitudes are then measured at each flow speed. The other type of VIV experiment is called forced vibration experiments. In this type of experiment the cylinder is forced to vibrate at a certain amplitude and frequency. The fluid forces are then measured under these conditions.

2.2.1 Free vibration experiments

Available results from free vibration experiments are that of Khalak & Williamson who did their experiments in water and the experiments done by Feng who did his experiment in air.

The results of free vibration experiments are typically presented in graphs with the dimensionless amplitude (Y/D) of vibration versus the reduced velocity,V_n given by equation (2.3).

$$V_n = \frac{V}{f_n \cdot D} \tag{2.3}$$

Here, V is the undisturbed flow velocity. f_n is the undamped natural frequency of the spring mounted system and D the diameter of the cylinder.

Figure 2-6, shows the results of the free vibration experiments from Khalak (water) and Feng (air). It is important to notice that the maximum amplitude for the experiments in water is much greater than that of air. Other observations are the large amplitudes observed over a wider range in the experiments of water than that of air.

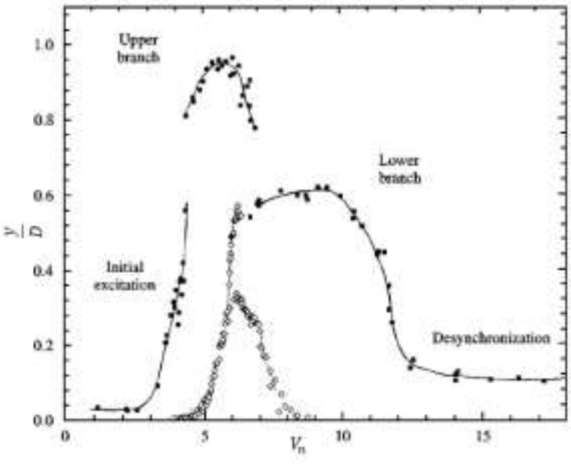

Figure 2-6: VIV response experiments in Khalak (▪) and Feng(◊) (Gabbai & Benaroya, 2005)

Lock in:

When the vortex shedding frequency comes close to the natural frequency of the spring mounted system the Strouhal law is no longer valid. However, the frequency of vortex shedding ‘locks’ on the natural frequency of the system. A cylinder is said to be in ‘lock in’ when the frequency of vortex shedding is equal to the natural frequency of the system. This happens for a certain range of velocities and is called the 'lock in range'. It is also in this 'lock in range' that VIV occur and the cylinders vibration amplitude is strongly amplified.

An important parameter for the lock in behavior of the experiment is the mass ratio. This is the ratio between the mass of the cylinder and the mass of the fluid surrounding the cylinder. Equation (2.4) gives an expression for the mass ratio, m^*

$$m^* = \frac{m}{\frac{\pi}{4}\rho D^2 L} \tag{2.4}$$

Where:

m = Mass of the cylinder
ρ = Density of the surrounding fluid
L = Length of the cylinder
D = Diameter of the cylinder

Generally speaking, the mass ratio in water is low and the mass ratio in air is high. This comes because of the higher density of water compared to air. R.D. Gabbai and H.Benaroya (Gabbai & Benaroya, 2005) make a distinction between the amplitude responses, a high -$m^*\zeta$ type and a low-$m^*\zeta$ type. The difference between the two amplitude responses is given schematically by Figure 2-7. Since systems that are submerged in air generally have higher mass ratio's than those submerged in water, it can be said that for experiments in air we have the high $m^*\zeta$ type response and experiments conducted in water the low $m^*\zeta$ type response. Not only the amplitude response is different but also the frequency of vibration. In systems with a low mass ratio the added mass influences the natural frequency of the system. This results in vibrations at a different frequency than the natural frequency. This phenomenon is called "synchronization". While on the other hand the added mass has no significant influence for systems with a high mass ratio. The frequency of vibration is than entrained by the natural frequency.

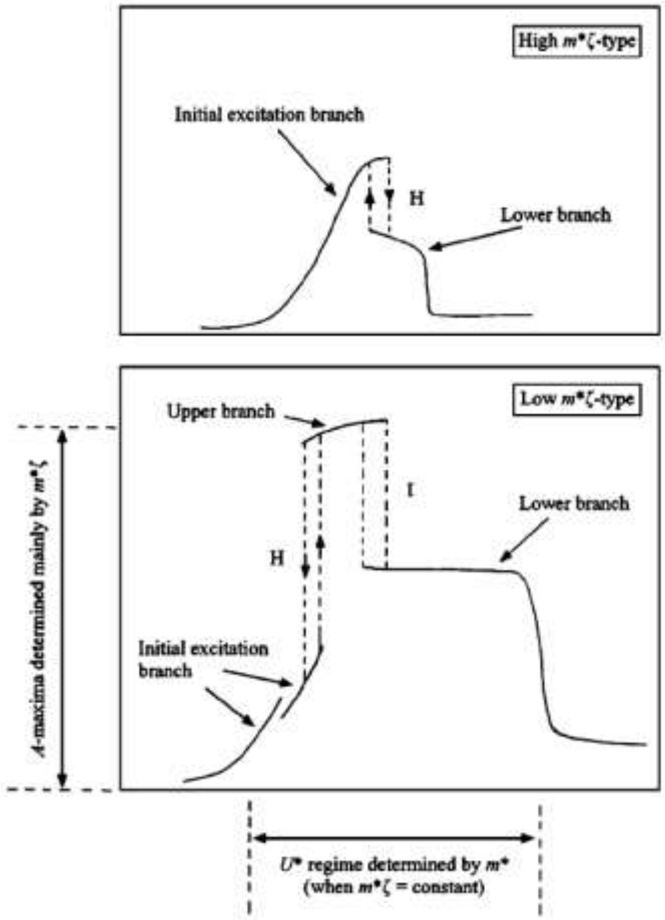

Figure 2-7 Difference between high m and low m* amplitude response (Gabbai & Benaroya, 2005)*

2.3 Suppression measures against VIV

We have seen that large amplifications of the vibration amplitude can occur during VIV. Since we do not desire large vibration amplitudes in Offshore operations, we will take a look at different suppression measures against VIV.

For suppression measures against VIV we can make use of two kind of devices. The first are by aerodynamic or hydrodynamic means, here the flow field is disturbed and vortices are stopped or disturbed from shedding. The second kind of device that we can use is a mass tuned damper, here vortices will be shed but the energy of the vibration will be dissipated by a secondary oscillatory system.

Aerodynamic or hydrodynamic means:

Zdravkovic (Zdravkovich, 1981) made an overview and classified the aerodynamic and hydrodynamic means into three categories; (i) surface protrusions (ii) shrouds and (iii) near wake stabilizers.

- **Surface protrusions:**
  Helical strakes, wires studs and fins are some examples of surface protrusions. They affect the separation lines and separated layers which in turn denies vortices from being formed. Their application can be omnidirectional or unidirectional. Helical strakes are the most

common solution, this is due to the fact that they are easy to install and are robust. The main drawback of surface protrusions is the fact that they increase drag. Which in turn increases the static wind load.

- **Shrouds**
  Perforated shrouds, gauze shrouds axial rods and axial slats are some examples of shrouds. They affect the entrainment layers in such a degree that vortices are denied from forming. Shrouds require a lot of materials to be used and are therefore not very common.

- **Near wake stabilizers**
  Splitter plates, guiding vanes, base-bleeds are some examples of near wake stabilizers. They affect the confluence point making it impossible for vortices to be formed. A major drawback from near wake stabilizers is that a different wind induced vibration mechanism, known as galloping, might occur at higher current velocities.

Tuned mass damper

As mentioned earlier a tuned mass damper is a secondary oscillatory system which is attached to the structure. This device dissipates the energy in the system and as a result large oscillation are omitted. A tuned mass damper has the main advantage that it can be used for different kind of vibration mechanisms not only VIV. The main disadvantage however is that due to its size and weight this might be impractical.

2.4 Overview of modeling VIV

There are multiple approaches to model Vortex Induced Vibrations. A variation of modelling methods has been studied whereas the majority can be grouped into semi-empirical models and numerical methods (Gabbai & Benaroya, 2005).

The advantages and disadvantages of both models are listed below:

- Numerical methods i.e. Computational Fluid Dynamics
  - Advantage: A complete insight of the flow field is obtained.
  - Disadvantages: A large amount of computational capacity required also, high computational time to run a simulation, especially for high Reynolds numbers (as is the case here).
- Semi Empirical Models, this model mimics the behavior of a Vortex Induced Vibrations
  - Advantages: Less computational time needed, less computational limitations.
  - Disadvantage: No insight on the flow field

2.5 Wind velocity profile

Wind speeds at higher altitude are usually larger than windspeeds at the surface. The wind velocity is lower at the surface and increases exponentially with increasing height above the ground. This is due to the surface roughness of the landscape/sea. Modeling of the wind is usually done by the power law wind profile. The power law is given by (2.5)

$$v(z) = v_{10}\left(\frac{z}{10}\right)^{\alpha} \tag{2.5}$$

Here v_{10} is the mean wind speed at a reference height of 10m and α is the power law exponent, this depends on the surface type. In open seas for example, the surface roughness is much lower than that of land, α is 0.09. On land, α varies between 0.11 and 0.37.

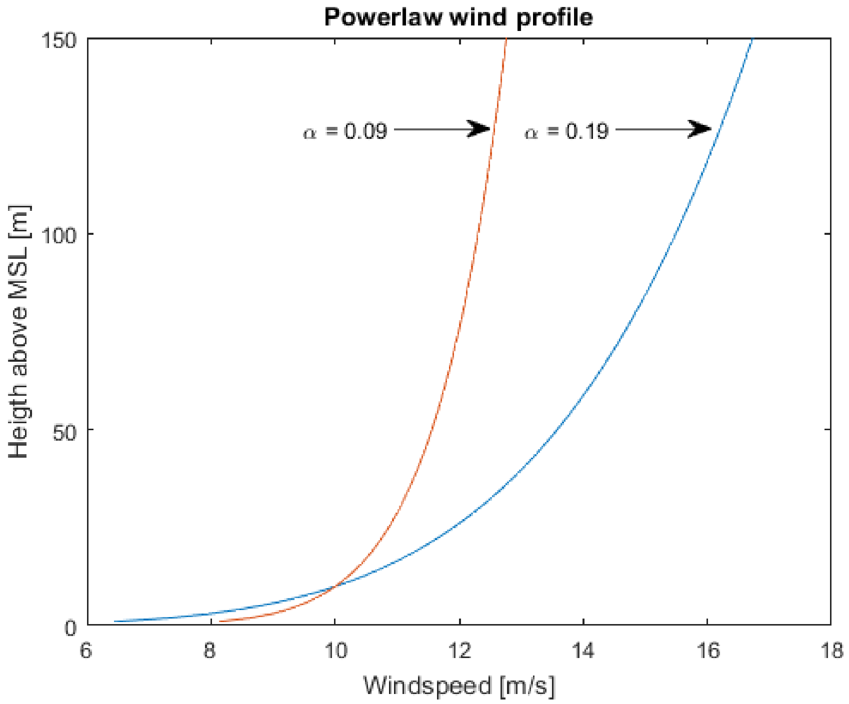

Figure 2-8 The power law wind profile with typical values of α.

Figure 2-8 shows the wind profile for different values of α. For lower values of α the profile is steeper and looks more uniform.

3 Wake oscillator modelling of rigid cylinders

Cylinders on viscoelastic supports are free to vibrate in fluid flow. Their motions effect the wake and influences the vortex lift force. When the vortex shedding frequency is close to the natural frequency of the viscoelastic system, the lift force and amplitude of vibration of the system starts to grows, until a steady state is reached. This behaviour is called self-excited and self-limiting. In order to model this effect, a coupled system between the equations of motions of the cylinder and a 'van der Poll' oscillator is used. The 'van der Poll' equation by nature also has this self-exciting and self-limiting effect.

This chapter starts with the derivation of the governing equations of a viscoelastic supported cylinder, then the coupling is made with the 'van der Poll' equation. Ultimately, the coupled system is tuned to model the free vibration experiments performed by Feng.

3.1 Governing equations of a spring mounted cylinder under vortex loading

To fully describe the motions of a cylinder under vortex loading some definitions are needed. Figure 3-1 is used to describe them. First, we need a reference system. Therefore, we introduce Y-axis and X-axis. The incoming flow, V is in-line with the X-direction and therefore we call X the in-line direction. Y is then called the cross-flow direction. The cylinder itself is moving with velocities $\frac{dX}{dt}$ in the in-line direction and $\frac{dY}{dt}$ in the cross-flow direction. Thus, the cylinder experiences a relative flow-velocity, called U which is composed of an in-line component, U_x. And a cross-flow component,U_y . The relative velocity can then be calculated by $U = \sqrt{U_x^2 + U_y^2}$ with $U_x = V - \frac{dX}{dt}$ and $U_y = \frac{dY}{dt}$.

Finally, the angle between U and V is defined by β.

Note that: $sin\beta = \frac{U_y}{U}$ and $cos\beta = \frac{U_x}{U}$

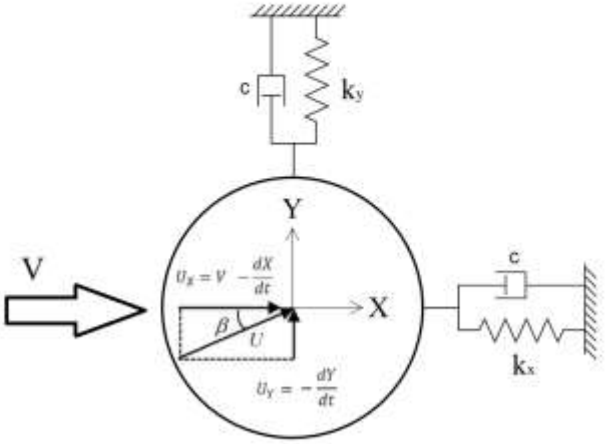

Figure 3-1 Cross sectional view of a cylinder on viscoelastic supports

Now that flow velocities are defined, we can take a look at the fluid forces acting on the system. Figure 3-2 shows the forces acting on the cylinder. We start with the forces proportional to the relative velocity the vortex drag force, F_{VD}, is in-line with the relative velocity and the vortex lift force $F_{VL}$is perpendicular to the drag force. Then the total crossflow force F_{VY} and the in-line force F_{VX} are both composed out of a drag part and a lift part.

$$F_{VY} = F_{VD} sin\beta + F_{VL} \cos\beta \tag{3.1}$$

$$F_{VX} = F_{VD} \cos\beta - F_{VL} sin\beta \tag{3.2}$$

Expressing the forces as force coefficients to what velocity they are proportional to results in the following expressions.

$$\frac{1}{2}\rho DLV^2 C_{VY} = (C_{VD} sin\beta + C_{VL} \cos\beta) \frac{1}{2}\rho DLU^2 \tag{3.3}$$

$$\frac{1}{2}\rho DLV^2 C_{VX} = (C_{VD} \cos\beta - C_{VL} sin\beta)\ \frac{1}{2}\rho DLU^2 \tag{3.4}$$

So, the cross-flow and in-line force coefficients can be expressed as

$$C_{VY} = (C_{VD} sin\beta + C_{VL} \cos\beta) \frac{U^2}{V^2} \tag{3.5}$$

$$C_{VX} = (C_{VD} \cos\beta - C_{VL} sin\beta) \frac{U^2}{V^2} \tag{3.6}$$

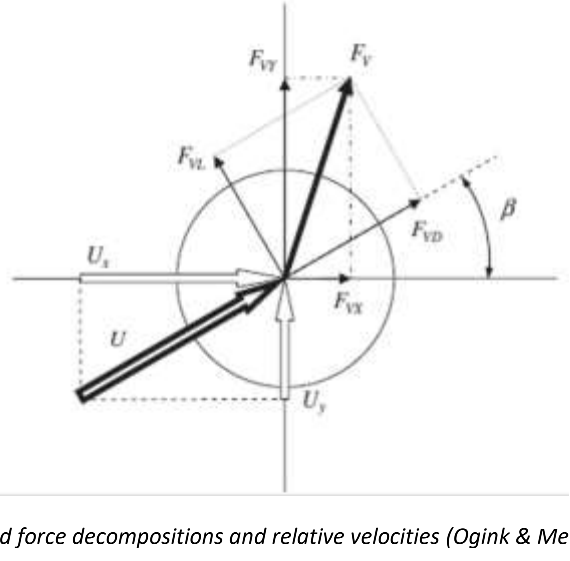

Figure 3-2 Fluid force decompositions and relative velocities (Ogink & Metrikine, 2010)

The equations of motion for the cylinder, which is allowed to move in both X, and Y directions are then given by the following set of equations.

$$(m + m_a)\frac{d^2Y}{dt^2} + c\frac{dY}{dt} + k_yY = \frac{1}{2}\rho DV^2LC_{VY} \tag{3.7}$$

$$(m + m_a)\frac{d^2X}{dt^2} + c\frac{dX}{dt} + k_xX = \frac{1}{2}\rho DV^2LC_{VX} \tag{3.8}$$

The equations of motions given by (3.7) and (3.8) are to be coupled to a Van der Pol oscillator in order to model the fluctuating lift force. But before doing that some important properties of the Van der Pol oscillator are discussed in the next subchapter.

3.2 Van der Pol oscillator

As stated before, vortex induced vibrations have some characteristics that the 'Van der Pol' equation can describe. Both are self-excited, but also self-limiting systems. The 'Van der Pol' oscillator is given below. Here the natural frequency of the oscillator is chosen to be equal to the vortex shedding frequency.

$$\frac{d^2q}{dt^2} + \epsilon\omega_s(q^2 - 1)\frac{dq}{dt} + \omega_s^2q = f(t) \tag{3.9}$$

Where: q , the wake parameter
ϵ, a tuning parameter
ω_s, the vortex shedding frequency

In the 'Van der Pol' equation the self-exciting self-limiting behaviour comes from the non-linear damping term, $\epsilon\omega_s(q^2 - 1)\frac{dq}{dt}$. For small values of q the damping term is negative, this means that there is energy input into the system (self-exciting). But when the value of q increases the damping term becomes positive and therefore energy is dissipated (self-limiting).

3.2.1 Unforced Van der Pol oscillator

The unforced 'Van der Pol' oscillator is given below.

$$\frac{d^2q}{dt^2} + \epsilon\omega_s(q^2 - 1)\frac{dq}{dt} + \omega_s^2q = 0 \tag{3.10}$$

To illustrate the self-limiting, self-exciting behaviour a simulation of an unforced 'Van der Pol' oscillator is done, see Figure 3-3 for the results. It shows that for a small initial displacement of $q(0) = 0.01$ the system will start to oscillate with increasing amplitude (self-exciting). After approximately 80 seconds the amplitude reaches a value of 2 where it no longer grows (self-limiting).

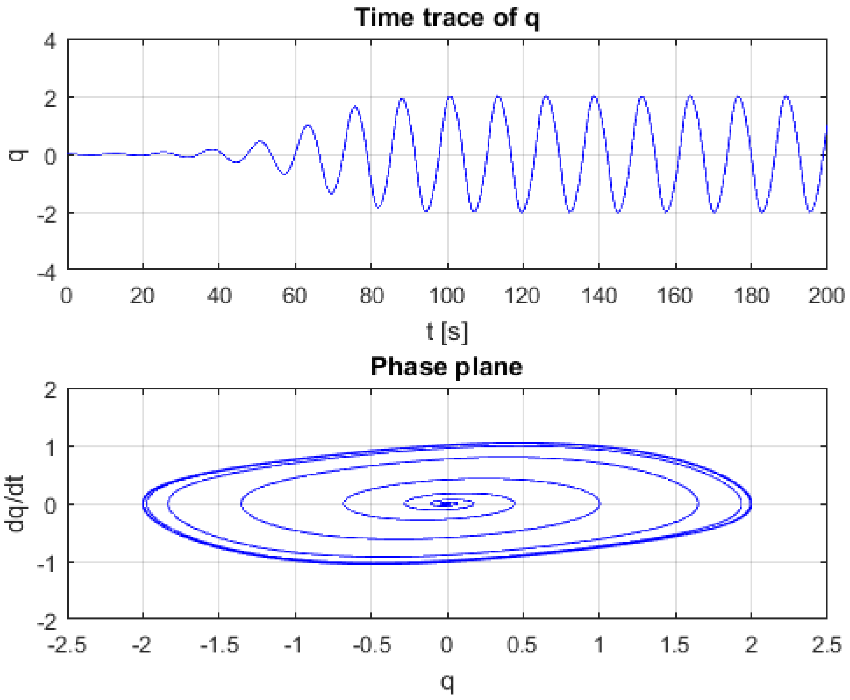

Figure 3-3 Time trace and Phase plane of an unforced Van der Pol oscillator with $\epsilon = 0.3$*,* $\omega_s = 0.5, q(0) = 0.01, \dot{q}(0) = 0$

The tuning parameter ϵ, is in fact a nonlinear damping coefficient. Higher values of ϵ results in more damping, which in turn causes a faster steady state. But also, an increase in non-linearity. Figure 3-4 demonstrates this statement. All other parameters are kept constant except ϵ , which is increased. In this case a steady state is reached after approximately 30 seconds. It is important to note that the oscillations are now less sinusoidal and start to behave more non-linear.

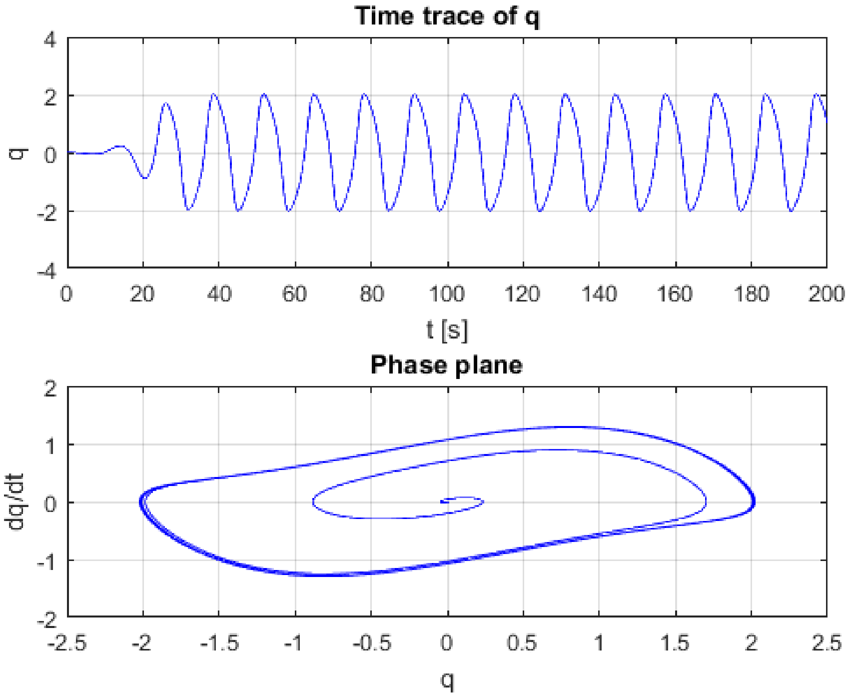

Figure 3-4 Time trace and Phase plane of an unforced van der pol oscillator with $\epsilon = 0.9$*,* $\omega_s = 0.5, q(0) = 0.01, \dot{q}(0) = 0$

3.2.2 Forced Van der Pol oscillator

The 'Van der Pol' oscillator can also describe the lock-in phenomenon of VIV. This can be illustrated by introducing a sinusoidal forcing term on the Van der Pol oscillator, the equation becomes as follows.

$$\frac{d^2q}{dt^2} + \epsilon\omega_s(q^2 - 1)\frac{dq}{dt} + \omega_s^2 q = A_f sin(\omega_f t) \tag{3.11}$$

Where: A_f , forcing amplitude
ω_f, forcing frequency

Lock-in occurs when the forcing frequency ω_f, is close to the "shedding frequency" ω_s. The vibration frequency of q then locks on the vibration frequency of the forcing. During lock-in there is also a strong amplification of q.

The phenomenon of lock-in will now be demonstrated by studying 3 cases:

- Case 1 $\omega_f = \omega_s$
- Case 2 $\omega_f = 2\omega_s$
- Case 3 $\omega_f = 3\omega_s$

All other parameters are kept constant during these cases. Figure 3-5, Figure 3-6 and Figure 3-7 show the results of these cases.

In case 1, a strong amplification of q is noticed. The exciting frequency and the natural frequency are the same, comparable to resonance. Since in the case both the vortex shedding and forcing frequencies are the same, q also vibrates at this frequency of 0.5 rad/s. It is interesting to see that at 1.5 rad/s and 2.5 rad/s there is also some energy observed. This is due to the non-linearity of the Van der Pol equation. In a linear system only, the exciting frequency would be observed in the steady state.

In case 2 the amplification already becomes less apparent. The dominant frequency is 1 rad/s and we can report that the vibration frequency is now locked on to the forcing frequency.

In case 3 the amplification is almost gone, and q starts to vibrate again at the 'vortex shedding frequency' of 0.5 rad/s. The exciting frequency and natural frequency of the oscillator are too far apart. The Van der Pol oscillator then oscillates once more at the vortex shedding frequency.

We can conclude, that lock-in indeed occurs when the frequency of forcing is close to the vortex shedding frequency. When the forcing frequency becomes too large, the lock in behaviour is not observed anymore. Furthermore, an increase of the forcing amplitude ,A, generally results in a larger amplification during lock-in. This is not demonstrated with the simulations done at this time.

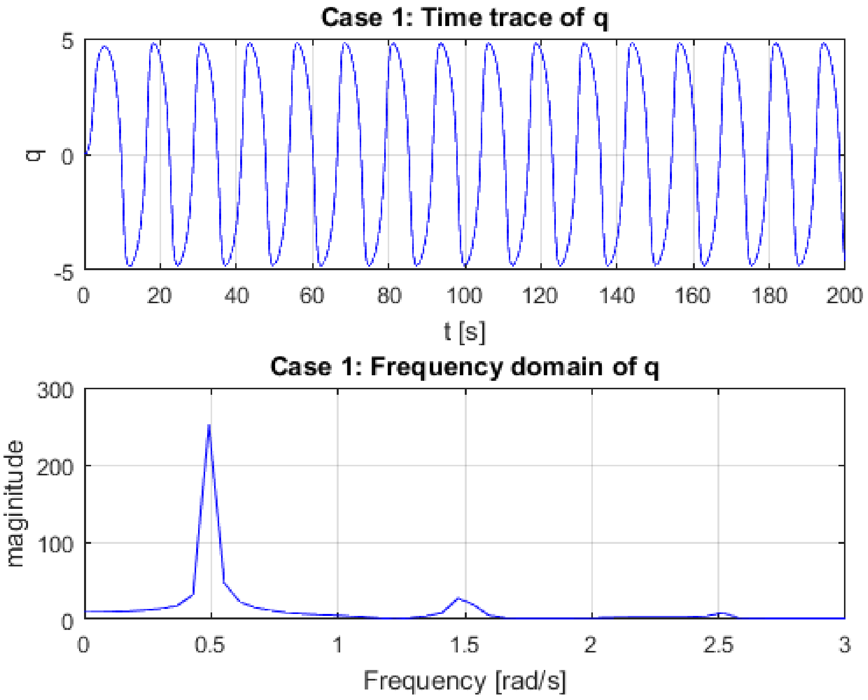

Figure 3-5 Time trace and Frequency domain of a forced Van der Pol oscillator with $\epsilon = 0.3$, $\omega_s = 0.5, q(0) = 0.01, \dot{q}(0) = 0$, *A=2 and* $\omega_f = 0.5$

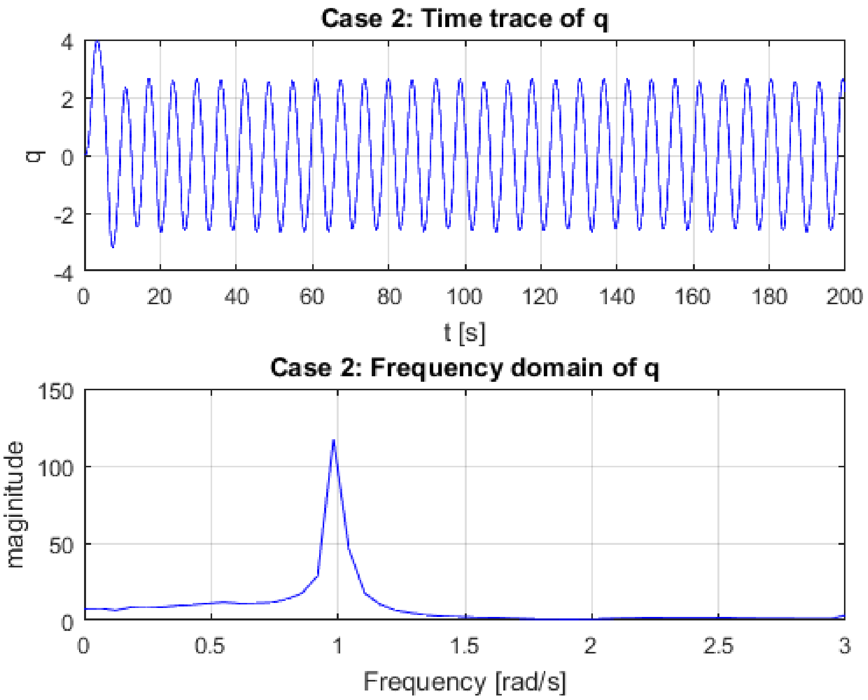

Figure 3-6 Time trace and Frequency domain of a forced Van der Pol oscillator with $\epsilon = 0.3$, $\omega_s = 0.5, q(0) = 0.01, \dot{q}(0) = 0$, *A=2 and* $\omega_f = 1$

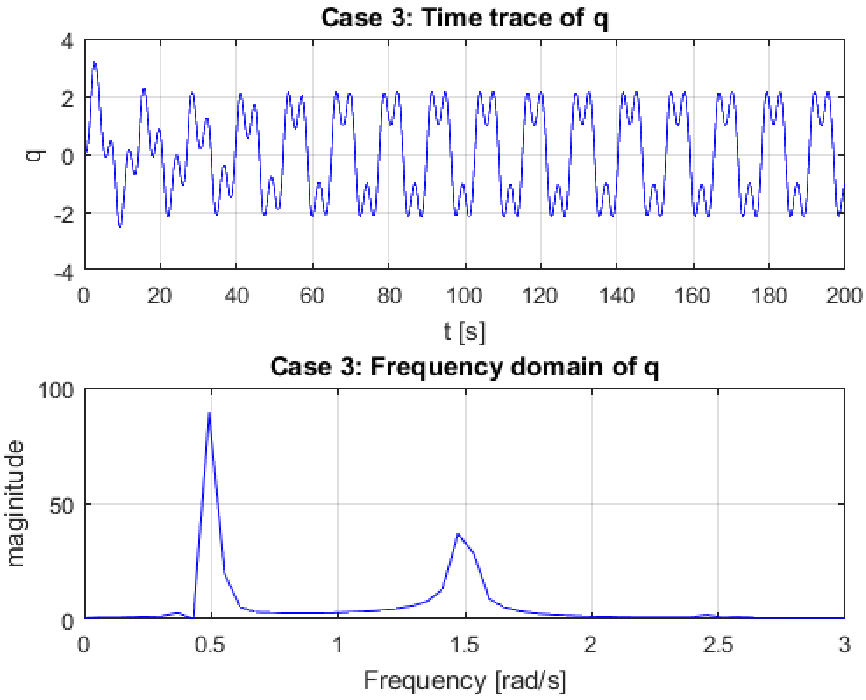

Figure 3-7 Time trace and Frequency domain of a forced Van der Pol oscillator with $\epsilon = 0.3$, $\omega_s = 0.5, q(0) = 0.01, \dot{q}(0) = 0$, *A=2 and* $\omega_f = 1.5$

3.3 Coupled system

In this section the Van der Pol oscillator will be coupled to the equation of motions of a cylinder on viscoelastic supports. Following the model of Ogink and Metrikine (2010) we will assume a linear acceleration coupling. This results in the following set of coupled differential equations:

$$(m + m_a)\frac{d^2Y}{dt^2} + c\frac{dY}{dt} + k_y Y = \frac{1}{2}\rho D V^2 L C_{VY} \tag{3.12}$$

$$(m + m_a)\frac{d^2X}{dt^2} + c\frac{dX}{dt} + k_x X = \frac{1}{2}\rho D V^2 L C_{VX} \tag{3.13}$$

$$\frac{d^2q}{dt^2} + \epsilon\omega_s(q^2 - 1)\frac{dq}{dt} + \omega_s^2 q = A\,\frac{d^2Y}{dt^2} \tag{3.14}$$

Ogink and Metrikine introduced the following equalities, which allows to write the problem statement in a non-dimensional form.

$$\tau = \ \omega_s t, \mathrm{T} = \omega_s T, \Omega = \frac{\omega}{\omega_s} = \frac{f}{f_s}; y = \frac{Y}{D}; x = \frac{X}{D} \tag{3.15}$$

Substituting the expressions (3.15) into the coupled system given by (3.12)(3.13)(3.14) results into a set of equations in the dimensionless form:

$$\ddot{y} + 2\zeta\Omega_{ny}\dot{y} + \Omega_{ny}^2 y = \frac{\rho D^2 L}{(m + m_a)} \frac{1}{8\pi^2 St^2} C_{vy} \tag{3.18}$$

$$\ddot{x} + 2\zeta\Omega_{nx}\dot{x} + \Omega_{nx}^2 x = \frac{\rho D^2 L}{(m + m_a)} \frac{1}{8\pi^2 St^2} C_{vx} \tag{3.19}$$

$$\ddot{q} + \epsilon(q^2 - 1)\dot{q} + q = A\ddot{y} \tag{3.20}$$

Here the over dots ($\dot{}$) represent the derivative to the dimensionless time τ.

In the dimensionless form the force coefficients are then given by.

$$C_{VY} = \left(C_{VD}(-2\pi St\dot{y}) + C_{VL}(1 - 2\pi St\dot{x})\right)\sqrt{(1 - 2\pi St\dot{x})^2 + (-2\pi St\dot{y})^2} \tag{3.21}$$

$$C_{VX} = \left(C_{VD}(1 - 2\pi St\dot{x}) - C_{VL}(-2\pi St\dot{y})\right)\sqrt{(1 - 2\pi St\dot{x})^2 + (-2\pi St\dot{y})^2} \tag{3.22}$$

At last the coupling between the Van der Pol oscillator and the lift force is done. Following the paper of Ogink and Metrikine (2010), the drag force is assumed to be constant and there is a linear relation between the lift force and the van der pol oscillator. This results in:

$$C_{VD} = C_{Do}, C_{VL} = \frac{C_{Lo}}{2} q \tag{3.23}$$

Now all that is left is to do is to tune the model to experiments conducted in air. This will be done in the next section.

3.4 Tuning to free vibrations experiments in air

In this research the interest goes to vortex induced vibrations in air. Therefore, it is needed to tune the wake-oscillator model to obtained results in air. Unfortunately, in literature, the available free vibration experiments conducted in air are generally speaking in the subcritical range. Whereas our Reynolds of interest are in the supercritical/ trans critical range. However, we still continued with this research and neglected the Reynolds number dependency for now. Therefore, the wake-oscillator model is tuned to experiments of Feng (1968), who also conducted his experiments in the subcritical range.

3.4.1 Feng free vibrations experiments

Feng conducted free vibration experiments in a low speed wind-tunnel. This was done for rigid circular cylinders and D-section cylinders free to vibrate in the crossflow direction. These experiments were conducted with different levels of damping. The focus in this thesis will be on circular cross-section cylinders with low damping. Table 3-1 gives a summary of the important properties from the experiment of Feng.

Table 3-1 Properties of the experiments of Feng (low damping case circular cross section)

Mass ratio	m^*	247
Damping ratio	ζ	0.00103
Reynolds number	Re	10^4- $4\text{x}10^4$ (Subcritical range)
Strouhal number	St	0.198
Stationary lift force coefficient	C_{LO}	0.315
Stationary drag force coefficient	C_{DO}	1.2*

(*) It has to be noted that the stationary drag coefficient was not found in the report from Feng, and this is assumed to be 1.2, which is a common value for stationary smooth cylinders in the subcritical range.

3.4.2 Simulation of Feng experiments

Since the experiments of Feng where only free to vibrate in the crossflow direction, the governing equations are reduced to equations (3.24) and (3.25).

$$\ddot{y} + 2\zeta\Omega_n\dot{y} + \Omega_n^2 y = \frac{1}{(m^* + C_a)}\frac{1}{2\pi^3 St^2}C_{vy} \tag{3.24}$$

$$\ddot{q} + \epsilon(q^2 - 1)\dot{q} + q = A\ddot{y} \tag{3.25}$$

The crossflow force coefficient is then given by

$$C_{VY} = \left(C_{D0}(-2\pi St\dot{y}) + \frac{C_{L0}}{2}q\right)\sqrt{1 + 4\pi^2 St^2(\dot{y})^2} \tag{3.26}$$

For tuning, the same methodology from Ogink & Metrikine (2010) was followed. The coupled system was solved using the ODE 23T solver from MATLAB, which is based on an explicit Runge-Kutta method.

The reduced velocity, V_n is systematically increased in steps of 0.1 from $V_n = 2 - 10$. Each simulation was done for 2000 units of the dimensionless time,τ. This is chosen such so there is enough time to reach steady state. After reaching the steady state, the amplitude of vibration was read. The highest peak in frequency domain is read as the cylinder vibration frequency. The initial conditions at $V_n = 2$ were as follows: $y(0) = \dot{y}(0) = \dot{q}(0) = 0$ and $q(0) = 0.01$. For all the other reduced velocities the “end condition” from the previous step is taken as the initial condition for the next simulation.

Following the methodology above different tuning parameters where tested. As first try, the values found by Ogink and Metrikine (2010) were tested. It is found that they both failed to predict the initial branch (Figure 3-8 (a)) and the lower branch (Figure 3-8 (b)) of the Feng experiments. This means that the tuning parameters from the other experiments are not valid for our experiment and there is a need for new parameters.

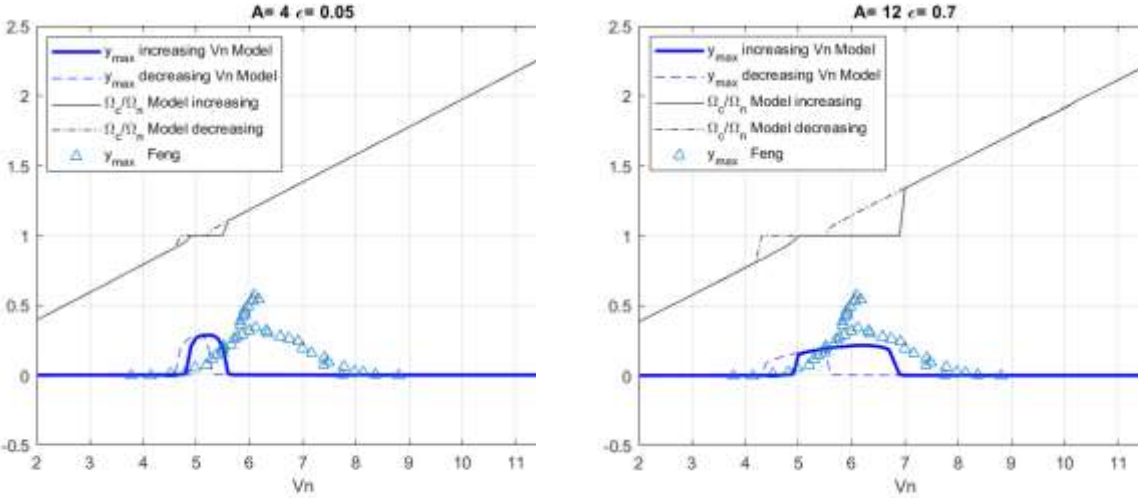

(a) (b)

Figure 3-8 Tuning parameters of Ogink and Metrikine

After which an alternative attempt is made by choosing the proposed values from Fachinetti, Figure 3-9 (a). It was found that the observed lock-in range is also underpredicted.

Finally, after trial and error, a good agreement is found for $A = 16$ and $\epsilon = 0.4$(Figure 3-9 b), the model has an agreeable prediction of the lower branch. Therefore, these are the values that will be used in the further research. The lock-in range for these parameters is found with a reduced velocity between 4.1 and 7.1.

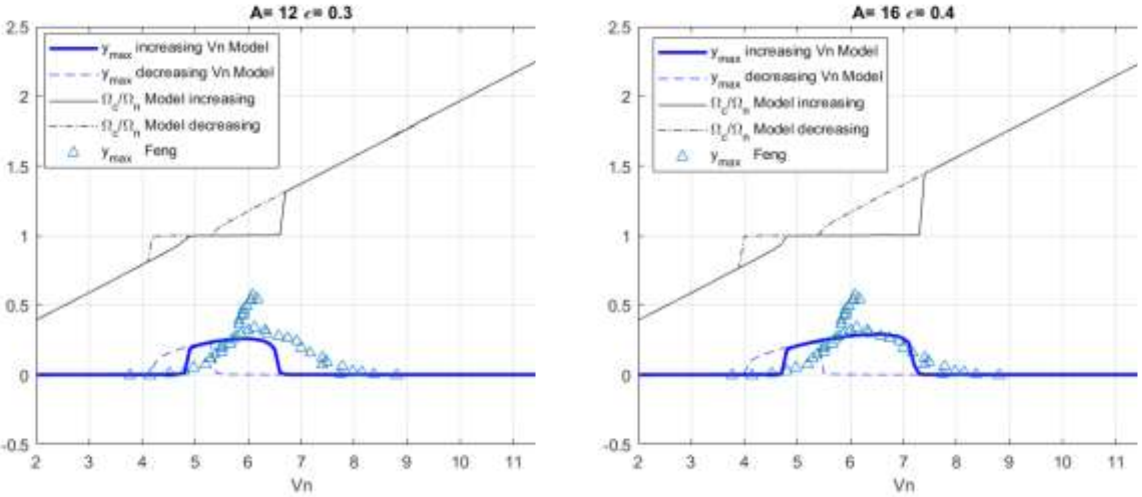

(a) (b)

Figure 3-9 Wake oscillator model, with different tuning parameters compared with the results from Feng

4 Wake oscillator modelling of flexible cylindrical structures

In chapter three the modelling of VIV of rigid cylinders in wind tunnel experiments by the wake oscillator model is given. However, wind turbine towers are not rigid, but rather flexible cylindrical structures. For that reason, an extension will be made in this chapter where the tower is modeled by a cantilever Euler Bernoulli beam under compression. The Euler-Bernoulli beam model is assumed to be a correct model since the length of the towers in consideration is much larger than the diameter. Then, for validation purposes the measured crossflow amplitude of a real-life chimney will be compared with that of two simulation runs.

4.1 Governing Equations

4.1.1 Equations of motions

The equations of motion for a Euler-Bernoulli beam under vortex loading in the cross-flow direction is given by equation (4.1). The in-line equation of motion under vortex loading is then given by equation (4.2). Following chapter 3.3, use is made of linear acceleration coupling with the cross-flow motion. The wake oscillator equation is then given by equation (4.3).

$$m(z)\frac{\partial^2 Y(z,t)}{\partial t^2}+\frac{\partial^2}{\partial z^2}\left(E^*I(z)\frac{\partial^2 Y(z,t)}{\partial z^2}\right)+\frac{\partial}{\partial z}\left(P(z)\frac{\partial Y(z,t)}{\partial z}\right)=\frac{1}{2}\rho D(z)V(z)^2C_{VY}(z) \tag{4.1}$$

$$m(z)\frac{\partial^2 X(z,t)}{\partial t^2}+\frac{\partial^2}{\partial z^2}\left(E^*I(z)\frac{\partial^2 X(z,t)}{\partial z^2}\right)+\frac{\partial}{\partial z}\left(P(z)\frac{\partial X(z,t)}{\partial z}\right)=\frac{1}{2}\rho D(z)V(z)^2C_{VX}(z) \tag{4.2}$$

$$\frac{\partial^2 q(z,t)}{\partial t^2}+\epsilon\omega_s(z)(q(z,t)^2-1)\frac{\partial q(z,t)}{\partial t}+\omega_s^2(z)q(z,t)=\frac{A}{D(z)}\frac{\partial^2 Y(z,t)}{\partial t^2} \tag{4.3}$$

The first term in the crossflow equation of motion, $m(z)\frac{\partial^2 Y(z,t)}{\partial t^2}$, is the inertia term where the mass per unit length $m(z)$ is a function of the height. The second term, $\frac{\partial^2}{\partial z^2}\left(E^*I(z)\frac{\partial^2 Y(z,t)}{\partial z^2}\right)$, is the bending restoring force. It is important to notice that at this point damping is considered by introducing E^*, with $E^* = E(1+a_1\frac{\partial}{\partial t})$ where a_1 is the proportional damping coefficient. The third term in the equation of motion takes compression into account. The compression is a function of the height and is given by $P(z) = m(z)(L-z)g$.

Notes:

- For brevity the terms in the in-line equation of motion are not explained but they are exactly the same.
- It is also important to note that since the wake parameter q, becomes a function of time and space, it is now being expressed as a partial differential equation.

4.1.2 Boundary conditions cantilever beam

In order to model the boundaries of the beam, boundary conditions are required. From the Euler-Bernoulli beam theory it is known that at each end we need two boundary conditions per direction. Since our beam is free to move in two directions (cross-flow and in-line) four boundary conditions are essential in each end. This means 8 boundary conditions are obtained in total. The boundary conditions for a cantilever beam are given as follows.

Fixed-Fixed on bottom:

In this boundary condition the rotation and transverse motion at the bottom are restricted. This condition will be used in situations where the connection with the soil or deck is considered as infinite stiff. In the continuous form the boundary conditions are given as follows.

- $At\ z = 0$

Cross-flow direction:

$$Y(0,t) = 0$$

This boundary condition states that the base of the beam (at the bottom) does not experience any displacement in the cross-flow direction.

(4.4)

$$\left.\frac{\partial Y(z,t)}{\partial z}\right|_{z=0} = 0$$

This boundary condition states that the base of the beam (at the ground) does not experience any rotation over the X-axis.

In-line direction:

$$X(0,t) = 0$$

This boundary condition states that the base of the beam (at the ground) does not experience any displacement in the in-line direction.

(4.5)

$$\left.\frac{\partial X(z,t)}{\partial z}\right|_{z=0} = 0$$

This boundary condition states that the base of the beam (at the ground) does not experience any rotation over the Y-axis.

Free on top:

This boundary condition is used when the top end of the structure is free. At this point there is no moment and similarly no shear force. In the continuous form the boundary conditions are written as follows.

- $At\ z = L$

Crossflow direction:

$$\left.E^{*}I(L)\frac{\partial^2 Y(z,t)}{\partial z^2}\right|_{z=L} = 0$$

This boundary condition models the assumption that there is no bending moment at the free end of the beam over the X-axis.

(4.6)

$$\left.\frac{\partial}{\partial z}\left(E^{*}I(L)\frac{\partial^2 Y(z,t)}{\partial z^2}\right)\right|_{z=L} = 0$$

This boundary condition models the assumption that there is no shearing force acting at the free end of the beam in the cross-flow direction.

Inline direction:

$$E^*I(L)\frac{\partial^2 X(z,t)}{\partial z^2}\bigg|_{z=L} = 0$$

This boundary condition models the assumption that there is no bending moment at the free end of the beam over the Y-axis.

$$\frac{\partial}{\partial z}(E^*I(L)\frac{\partial^2 X(z,t)}{\partial z^2})\bigg|_{z=L} = 0 \tag{4.7}$$

This boundary condition models the assumption that there is no shearing force acting at the free end of the beam in the in-line direction.

4.2 Numerical implementation

In this thesis an ordinary differential equation (ODE) solver of MATLAB is used for solving the set of equations described in chapter 4.1. Normally the MATLAB ODE solvers can only solve first order equations. Since the equation of motion for a Euler Bernoulli beam is of a higher order partial differential equation (PDE), we first need to write the higher order PDE as a set of first order ODE's in order to implement this in the ODE solver from MATLAB. This is done by discretizing the equation of motion. Hence, the discretization technique will be explained in this section. This will be followed by discretization of the internal domain and the used boundary conditions.

4.2.1 Discretization method

Numerous discretization techniques are available, in this thesis the finite difference method was used because of its straight forward implementation of the derivatives. The finite difference method makes use of the Taylor series expansion to estimate the derivatives. The first four derivatives with a second order accuracy are given by equations (4.8).

$$\begin{gathered}
\frac{\partial Y_i}{\partial z} = \frac{1}{2\Delta z}(Y_{i+1} - Y_{i-1}) \\
\frac{\partial^2 Y_i}{\partial z^2} = \frac{1}{(\Delta z)^2}(Y_{i+1} - 2Y_i + Y_{i-1}) \\
\frac{\partial^3 Y_i}{\partial z^3} = \frac{1}{2(\Delta z)^3}(Y_{i+2} - 2Y_{i+1} + 2Y_{i-1} - Y_{i-2}) \\
\frac{\partial^4 Y_i}{\partial z^4} = \frac{1}{(\Delta z)^4}(Y_{i+2} - 4Y_{i+1} + 6Y_i - 4Y_{i-1} + Y_{i-2})
\end{gathered} \tag{4.8}$$

Where, i indicates the node number. This goes from 1 to the chosen number of discretization points, n. Here, Δz is the element length.

4.2.2 Discretization of the internal domain

The equation of motion for a Euler-Bernoulli beam under compression is given by.

$$\rho A(z)\ \frac{\partial^2 Y(z,t)}{\partial t^2} + \frac{\partial^2}{\partial z^2}\left(E^*I(z)\frac{\partial^2 Y(z,t)}{\partial z^2}\right) + \frac{\partial}{\partial z}\left(P(z)\frac{\partial Y(z,t)}{\partial z}\right) = f_{extern} \tag{4.9}$$

Rewriting equation (4.9) results in:

$$\begin{aligned}\rho A\ddot{Y} + \alpha EI\dot{Y}'''' + 2\alpha EI'\dot{Y}''' + \alpha EI''\dot{Y}'' + EIY'''' + 2EI'Y''' + EI''Y'' + PY'' + P'Y' \\ = f_{extern}\end{aligned} \tag{4.10}$$

Substituting the finite differences derivatives into the equation of motion given by (4.10) and assuming that the derivatives I', I'' and P' are known from the geometry of the beam. We obtain a second order ODE of an arbitrary node i.

$$\begin{gathered}\rho A_i\ddot{Y}_i + \alpha\frac{EI_i}{\Delta z^4}\left(\dot{Y}_{i-2} - 4\dot{Y}_{i-1} + 6\dot{Y}_i - 4\dot{Y}_{i+1} + \dot{Y}_{i+2}\right) + \\ \frac{2\alpha EI_i'}{2\Delta z^3}\left(-\dot{Y}_{i-2} + 2\dot{Y}_{i-1} + 0\dot{Y}_i - 2\dot{Y}_{i+1} + \dot{Y}_{i+2}\right) + \\ \frac{\alpha EI_i''}{\Delta z^2}\left(\dot{Y}_{i-1} - 2\dot{Y}_i + \dot{Y}_{i+1}\right) + \\ \frac{EI_i}{\Delta z^4}(Y_{i-2} - 4Y_{i-1} + 6Y_i - 4Y_{i+1} + Y_{i+2}) + \\ \frac{2EI_i'}{2\Delta z^3}(-Y_{i-2} + 2Y_{i-1} + 0Y_i - 2Y_{i+1} + Y_{i+2}) + \\ \frac{EI_i''}{\Delta z^2}(Y_{i-1} - 2Y_i + Y_{i+1}) + \\ \frac{P_i}{\Delta z^2}(Y_{i-1} - 2Y_i + Y_{i+1}) \\ \frac{{P'}_i}{2\Delta z}(-Y_{i-1} + 0Y_i + Y_{i+1}) = f_{i_{extern}}\end{gathered} \tag{4.11}$$

Note that because of symmetry the in-line direction results in the same equation. For brevity it is not derived here.

With the higher order PDE written as a set of second order ODE's, all that is left to do is the implementation of the boundary conditions. This will be treated in the next section.

4.2.3 Discretization of the boundary conditions

Fixed-Fixed at bottom:

By substitution of the finite difference derivatives approximations into equations (4.4) we obtain the boundary condition in discretised form.

$$Y_0 = 0 \tag{4.12}$$

$$\frac{1}{2\Delta z}(Y_1 - Y_{-1}) = 0 \tag{4.13}$$

Notice that there is a need of a fictitious (Y_{-1}) node to describe the derivative at the boundary. By making use of equations (4.12) and (4.13) the fictitious node is expressed in terms of the real nodes.

$$Y_{-1} = Y_1 \tag{4.14}$$

Due to symmetry the X direction will be the same and for brevity it is not derived here.

Free at top:

Again, by substitution of the finite differences approximations into equation (4.6) we obtain the boundary condition in discretised form.

$$E^* I(L) \frac{1}{(\Delta \mathrm{z})^2} (Y_{N+1} - 2Y_N + Y_{N-1}) = 0 \tag{4.15}$$

$$E^* I(L) \frac{1}{2(\Delta \mathrm{z})^3} (Y_{N+2} - 2Y_{N+1} + 2Y_{N-1} - Y_{N-2}) = 0 \tag{4.16}$$

Notice that there is a need of 2 fictitious (Y_{N+1} *and* Y_{N+2}) nodes to describe the derivative at the boundary. By using equations (4.15) and (4.16) we can express the fictitious node in terms of the real nodes.

$$Y_{N+1} = 2Y_N - Y_{N-1} \tag{4.17}$$

$$Y_{N+2} = 4Y_N - 4Y_{N-1} + Y_{N-2} \tag{4.18}$$

Due to symmetry the X direction will be the same and for brevity it is not derived here.

4.3 Validation on Chimney

In this paragraph the model is validated by comparing the simulation results of the wake-oscillator model with the measurement results of an in situ chimney. The reason for using a chimney as validation is because of its fit, which is quite similar as an offshore wind turbine tower from the geometry point of view. They are both tall cylindrical structures. Further, model tests do not satisfy the full-scale Reynolds number. This is due to size restrictions in wind tunnels (Ruscheweyh & Galemann, 1996).

4.3.1 Info on Chimney and measurements results

Th. Galemann and H. Ruscheweyh (Galemann & Ruscheweyh, 1992) carefully measured the crossflow amplitude of an experimental chimney. The chimney in consideration is stationed in Aachen, Germany and measurements where performed in a period of 3 years. This experimental chimney is composed of steel, 28m in height and has an outer diameter of 0.914m. It has a smooth painted surface. The chimney is constructed out of 5 sections and with increasing height, the thickness decreases. The consequence of this is a chimney which is more flexible at the top. Table 4-1 gives an overview of the exact chimney dimensions. Since no information is provided about the material properties, such as the steel density and the Young's modulus, reasonable assumptions are made. The steel density is assumed to be 7800 kg/m^3 and the Young's modulus is assumed to be 200 GPa.

Table 4-1 Experimental Chimney dimensions at the sections

Section	Height[m]	Thickness[mm]	Diameter[mm]
1	0-5	12	914
2	5-10	10	914
3	10-14	8	914
4	14-19	4	914
5	19-28	3	914

Th. Galemann and H.Ruscheweyh (1992) stated a critical windspeed of 9m/s which corresponds to a Reynolds number of 5x 10^5. This Reynolds number is in the supercritical range. Referring to Table 2-1 we can see that the Reynolds number falls inside the typical values of the tower dimensions considered during operational conditions. It seems natural to work in the same Reynolds number range as that of the wind turbine towers, therefore this chimney is a good choice from the Reynolds number point of view. Furthermore, the researchers stated a logarithmic decrement of damping, δ of 0.012, it is assumed that this is for the first mode only. The fundamental natural frequency f_{n1} is 1.7 Hz.

The measured Strouhal number fluctuates between 0.16-0.26 with a frequent value of 0.21. This is an interesting observation, according to measurements on stationary smooth cylinders (Figure 2-5) we would expect a Strouhal number of around 0.4 in this Reynolds number range.

As mentioned before the crossflow measurements were done over a period of three years. Figure 4-1 shows the measurement result. In this period the maximum value of the crossflow vibrations was 0.14 diameters.

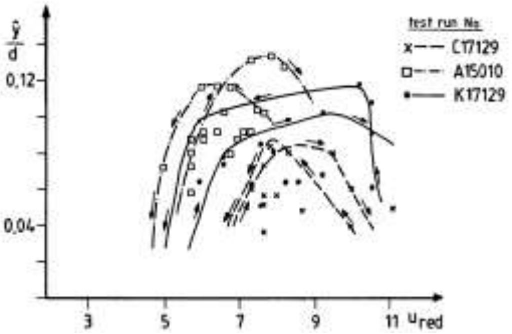

Figure 4-1 measurements of experimental chimney (Ruscheweyh & Galemann, 1996)

Table 4-2 gives a summary of the data of the experimental chimney.

Table 4-2 Experimental Chimney data

Height	h	28	m
Outer diameter	D_o	0.91	m
Density*	ρ_{st}	7800	Kg/m^3
Young's modulus*	E	200	GPa
Fundamental natural frequency	f_{n1}	1.7	Hz
Log. Decrement of damping first mode	δ_1	0.012	-
Critical wind speed at 10m	v_{crit}	9.0	m/s
Reynold at critical wind speed	Re	5x10^5	-
Measured Strouhal number	St	0.16-0.26	[-]
Measured crossflow amplitude	Y/D	0.14	[-]

(*) assumed values

4.3.2 Chimney study cases

Structural model chimney:

The Chimney is modeled as a cantilever Euler Bernoulli beam build out of 5 sections. Discretization of the beam is done by using the finite difference method.

At each interface there are 4 interface conditions in each direction. Since the interface conditions are the same at each interface, we will write down a general interface condition existing out of an upper beam and a lower beam. The interface conditions are then given by the following equations in the cross-flow direction:

$$\begin{gathered}
Y_L(Z_{inter}, t) = Y_U(Z_{inter}, t) \\
\left.\frac{\partial Y_L}{\partial z}\right|_{z=Z_{inter}} = \left.\frac{\partial Y_U}{\partial z}\right|_{z=Z_{inter}} \\
\left.E^* I_L(Z_{inter}) \frac{\partial^2 Y_L}{\partial z^2}\right|_{z=Z_{inter}} = \left.E^* I_U(Z_{inter}) \frac{\partial^2 Y_U}{\partial z^2}\right|_{z=Z_{inter}} \\
\left.\frac{\partial}{\partial z}\left(E^* I_L(Z_{inter}) \frac{\partial^2 Y_L(z,t)}{\partial z^2}\right)\right|_{z=Z_{inter}} = \left.\frac{\partial}{\partial z}\left(E^* I_U(Z_{inter}) \frac{\partial^2 Y_U(z,t)}{\partial z^2}\right)\right|_{z=Z_{inter}}
\end{gathered} \tag{4.19}$$

And in the in-line direction:

$$
\begin{aligned}
X_L(Z_{inter},t) &= X_U(Z_{inter},t) \\
\left.\frac{\partial X_L}{\partial z}\right|_{z=Z_{inter}} &= \left.\frac{\partial X_U}{\partial z}\right|_{z=Z_{inter}} \\
E^* I_L(Z_{inter})\left.\frac{\partial^2 X_L}{\partial z^2}\right|_{z=Z_{inter}} &= E^* I_U(Z_{inter})\left.\frac{\partial^2 X_U}{\partial z^2}\right|_{z=Z_{inter}} \\
\left.\frac{\partial}{\partial z}\left(E^* I_L(Z_{inter})\frac{\partial^2 X_L(z,t)}{\partial z^2}\right)\right|_{z=Z_{inter}} &= \left.\frac{\partial}{\partial z}\left(E^* I_U(Z_{inter})\frac{\partial^2 X_U(z,t)}{\partial z^2}\right)\right|_{z=Z_{inter}}
\end{aligned}
\tag{4.20}
$$

After discretization, the damping coefficient, $a_1$is set at 0.312X10^{-3}. By doing this a logarithmic decrement of damping of 0.012 is achieved in the first mode. This corresponds to the measurements of the in-field chimney. In the second mode the logarithmic decrement of damping then becomes 0.048. In the appendix a detailed explanation is given on determining the logarithmic decrement of damping.

Figure 4-2 shows the first three mode shapes together with first three undamped natural frequencies. It is important to note that there is a slight difference between the fundamental frequency of the in situ chimney and the fundamental frequency of the chimney model. This can be explained by the soil structure interaction which is neglected in the model. In the model the soil is modeled as infinitively stiff, but this cannot be correct since the soil should have some finite stiffness. This results in a natural frequency for the model that is slightly higher than that of the real chimney.

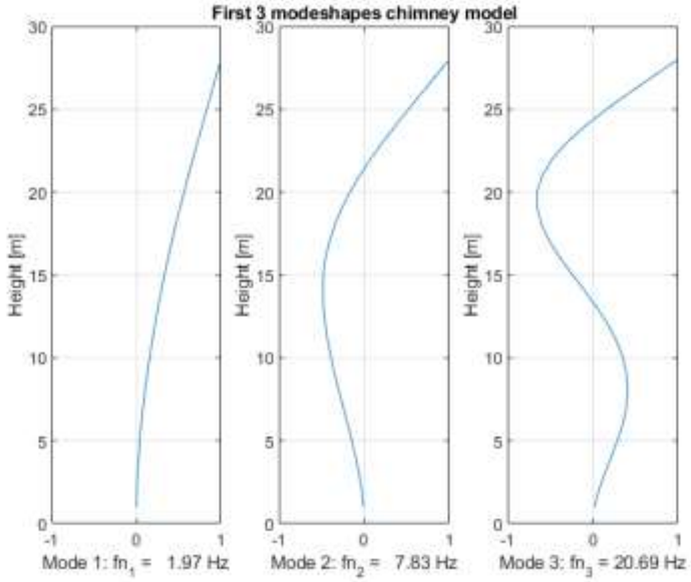

Figure 4-2 Mode shapes and natural frequencies real life chimney

Reduced velocity:

The wind is modeled with a power law profile. Making this a sheared wind. As a result of the sheared wind the reduced velocity is a function of the height and the natural frequency given by equation (4.21).

$$V_{n_i}(z) = \frac{V(z)}{fn_i D_o(z)} \tag{4.21}$$

Where,		
	$V_{n_i}(z)$	Is the reduced velocity
	i	Is the index noting the natural frequency
	fn_i	Is the natural frequency
	$V(z)$	Is the windspeed as function of the height
	$D_o(z)$	Is the outer diameter as function of the height

The wind power law coefficient, α, is set at 0.19 which corresponds to a slightly rough terrain on land.

Wake oscillator simulation:

For the simulations two cases were studied. This is done because no data was available of the stationary force coefficients.

- **Case I:**
  In case I the same parameters for the wake oscillator as used in the simulations for the Feng experiment in chapter 3.4.2 are. The stationary lift force, C_{LO} and stationary drag force coefficient,C_{DO} were respectively 0.315 and 1.2. It is important to remember that the Feng experiments where in the subcritical regime, while the chimney is in the critical regime. By doing this we totally neglect the Reynolds number dependency. This is considered an interesting case since the measured Strouhal number is around 0.21 instead of 0.4 in contrary to what we would expect in the critical range. Therefore, the assumption is made that the stationary drag and stationary lift coefficient will also follow the values found in subcritical range.

- **Case II:**
  In case II the stationary lift force, C_{LO} and stationary drag force coefficient,C_{DO} were read from the graphs in Figure 2-4. It is important to note that reading from these graphs is prone to errors. We estimated the stationary lift force coefficient at 0.1 and the stationary drag force coefficient 0.8. For the Strouhal number the measured value of 0.21 is used. By doing this the Reynolds number dependency is taken into consideration.

Further for both cases the coupling parameter, A and tuning parameter, ϵ are chosen respectively as 16 and 0.4.

Simulations where done for winds speeds from 1 m/s with increasing steps of 1m/s up till a maximum windspeed of 38 m/s at a reference height of 10m. At every windspeed the simulation is run for 500s of simulation time. This was sufficient to reach the steady state of vibration. At this point the steady state amplitude is measured. After which the windspeed is increased. At the “next windspeed” the steady state amplitude is measured once more and this is repeated until a velocity of 38m/s is reached. A summary of the simulation input is given in Table 4-3.

Table 4-3 Summery of Simulation input Chimney

		Case I	Case 2	
Coupling parameter	A	16	16	[-]
Tuning parameter	ϵ	0.4	0.4	[-]
Stationary lift force coefficient	C_{LO}	0.315	0.1	[-]
Stationary drag force coefficient	C_{DO}	1.2	0.8	[-]
Strouhal number	St	0.21	0.21	[-]
Windspeed at 10 m	v_{10}	1-38	1-38	[m/s]
Wind power law coefficient	α	0.19	0.19	[-]

Large oscillations are expected when a large part of the reduced velocity is within the lock-in range. In chapter 3.4.2 it was found that when the reduced velocity is between 4.1 and 7 lock-in occurs. Figure 4-3 shows that we can indeed expect large oscillations at the “critical windspeed” of 9 m/s at 10m since most part of the first reduced velocity is within the lock-in range. Looking at Figure 4-4 we see that again a large part the second reduced velocity is in the lock-in range. This means that we can also expect large oscillations at the maximum windspeed. It is interesting to observe that the reduced velocities do not intersect each other. This means we do not expect a multimode response but vibrations at one dominant frequency belonging to a particular mode.

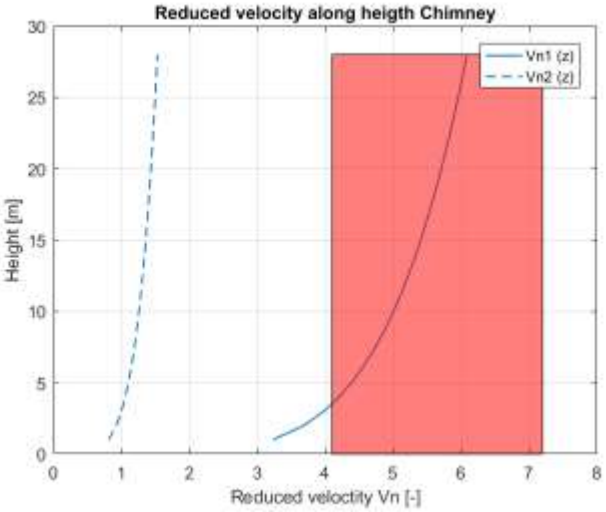

Figure 4-3 Reduced velocity of the chimney for 9m/s wind at 10m height

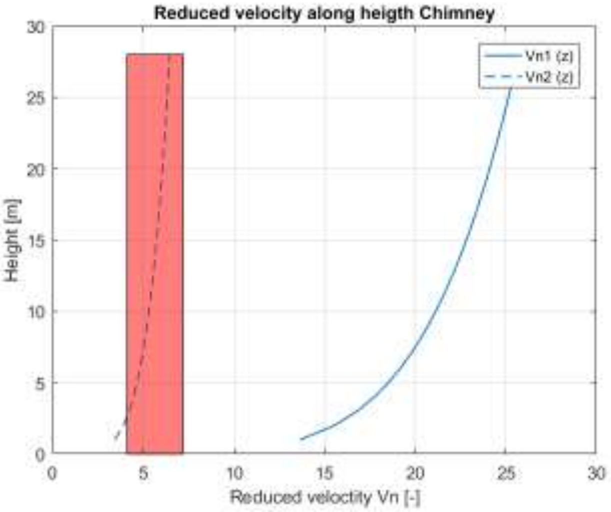

Figure 4-4Reduced velocity of the chimney for 38m/s wind at 10m height

Results

Figure 4-5 shows the tip crossflow amplitude against the windspeed at 10m height. At the “critical windspeed” of 9m/s, the model indeed predicts large oscillations for both cases. For case I the maximum value is around 11m/s with a vibration amplitude of 0.53 diameters which is much larger than the in situ measurements. The results of case II are more in line with the measurements. With a maximum cross-flow amplitude of 0.13 diameters at a windspeed of 9 m/s, this almost the same value of the measurement. This makes case II more representative. It is also important to note that for both cases VIV occurs again at higher windspeeds. This is according to expectation since at these windspeeds large parts of the second reduced velocity are in the lock-in range. These vibrations are expected to be in the second mode. In order to confirm this, it is also interesting to not only investigate the vibration amplitude, but also the frequency of vibration and the vibration envelopes.

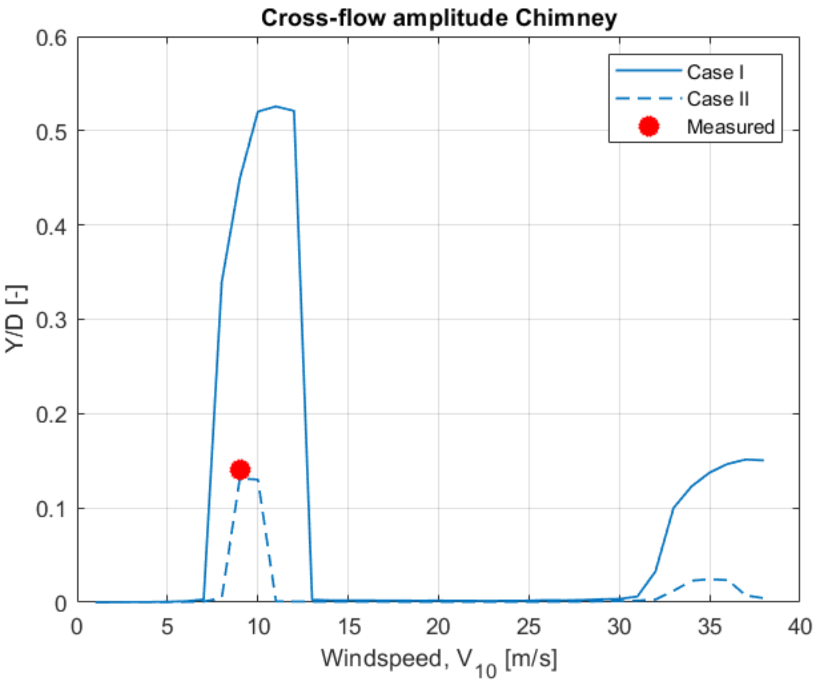

Figure 4-5 Simulation results of the Time traces of the tip displacement Real Life Chimney

- **Vibration envelopes and frequency Case I:**

Figure 4-6 shows the vibration envelopes at the windspeeds where the vibration amplitudes are the largest. It is obvious that at 11m/s the chimney is vibrating in the first mode only and at 38m/s in the second mode. In order to find the dominating vibration frequencies at the tip of the chimney a Fast Fourier Transformation is done, and then the power spectral density is plotted in Figure 4-7. We can see that the dominating frequency of vibration at the tip is 1.97 Hz at an wind speed of 11m/s. This is exactly at the first natural frequency. Further at a windspeed of 38m/s the dominating frequency at the tip is 7.86 Hz. This is almost exactly at the second natural frequency.

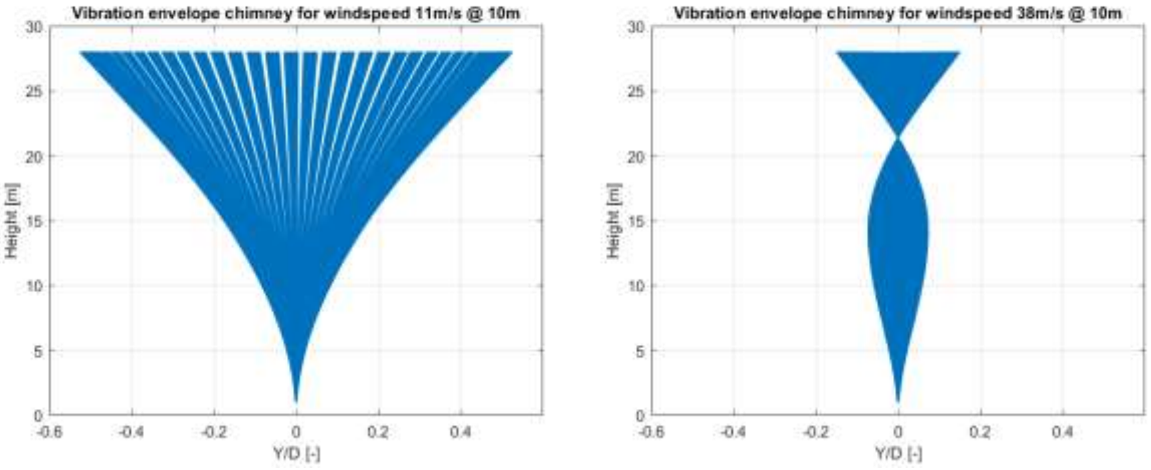

(a) (b)

Figure 4-6 Vibration Envelopes Case I

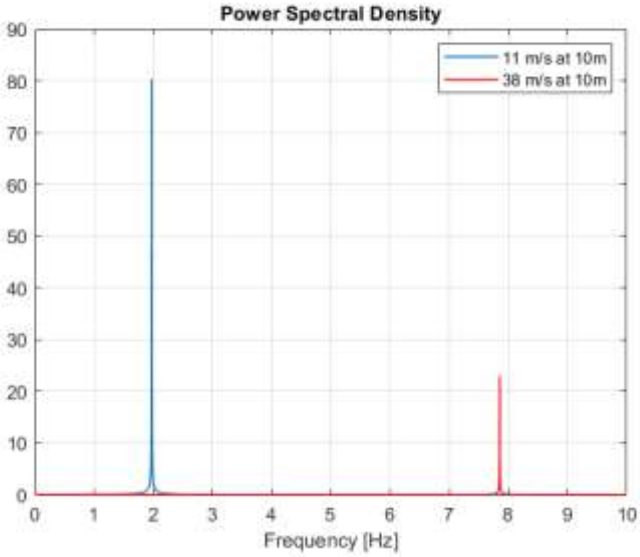

Figure 4-7 Power Spectral Density Case I

- **Vibration envelopes and frequency Case 2:**

Figure 4-8 (a) shows the vibration envelope at a windspeed of 9m/s at 10m height. At this windspeed it is obvious that the chimney is vibrating in the first mode only. Figure 4-8 (b) shows the vibration envelope at an windspeed of 35m/s. Whereas the chimney is vibrating in the second mode. The dominating vibration frequencies can be obtained from Figure 4-9. With 1.97 Hz at 9m/s and 7.84 Hz at 35 m/s they follow the natural frequencies.

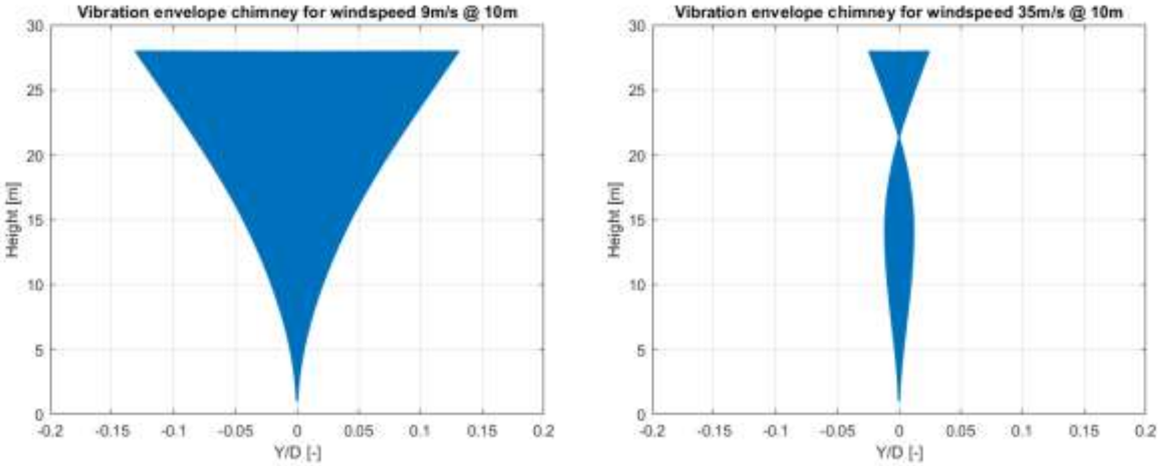

(a) (b)

Figure 4-8 Vibration envelopes Case II

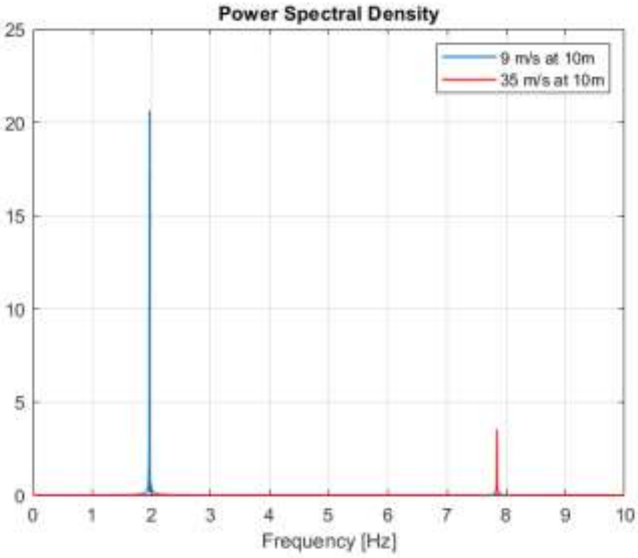

Figure 4-9 Power Spectral Density Case II

4.3.3 Conclusions on the chimney simulations

The chimney studied in this thesis was in the super critical flow regime according to the Reynolds number, here we would expect a Strouhal number of 0.4 for smooth stationary cylinders. But the measured Strouhal number had a frequent value of 0.21. This would suggest that the chimney is in the sub critical flow regime. This discrepancy can have two possible explanations. First is that the chimney was not that smooth. Second, the Strouhal number is different for flexible vibrating cylinders. Not knowing what force coefficients to use two cases where studied.

In case I the assumption was made that there was no Reynolds number dependency at all and that we use the force coefficients of the subcritical regime. But in the results, a discrepancy is found. The amplitude of vibration differs by a factor of approximately three. A possible explanation for this difference in vibration amplitude is that the Reynolds number is a significant parameter. The lift and drag force coefficients are much smaller in the critical and trans critical ranges. By neglecting the differences in lift and drag force coefficient the aerodynamic forces are too high. This results in an overprediction of the model.

In case II the Reynolds number dependency was introduced by taking the values of the stationary force coefficients in the correct flow regime. This resulted in a much better prediction by the model. Therefore, we conclude that we cannot neglect the Reynolds number dependency. However, this was done for only one chimney. In order to validate the use of these force coefficients different chimney measurement should be compared with the simulation results.

Further the phenomena of lock-in is captured by using this wake-oscillator model. Even though the chimney is excited with different frequencies coming from the sheared wind, the frequency of vibration matches the closest natural frequencies during lock-in.

Finally, it would be best to retune the model to a real-life situation but due to a lack of data we will continue using the tuning parameters from the Feng experiments further. The stationary force coefficients from case II will be used since these gave better results.

5 Study cases wind turbine towers

In this chapter, the model explained in chapter 4 will be used to simulate vortex induced vibrations of a wind turbine tower during different stages of transport. The first subchapter gives general information of a typical wind turbine tower and the wind conditions at sea. In the second subchapter chapter the structural modeling of the tower is explained. Then, in the third subchapter several study cases are done. Finally, with the knowledge obtained from the case study some conclusions are drawn.

5.1 General information

The parameters used for the case study in this thesis are based on an actual wind turbine installation project of Seafox. In this project a mass tuned damper was used on top of the towers as mitigation for VIV. However, due to practical limitations the mass tuned damper did not function properly during sailing.

5.1.1 Tower

The tower has an total height of 78 m and is build out of two sections, the bottom part of the tower is uniform with an outer diameter of 6m, while the top part is linearly tapered from 6m outer diameter to 4 m. The tapering starts at two third of the towers height. The thickness over the complete height of the tower is 0.035 m.

There is a mass on top of 9.5 tons which is in fact the mass tuned damper. Since this did not work during sailing it is considered as a rigid mass for all study cases, this can be seen as a conservative approach. A rigid mass on top of the tower will decrease the natural frequency and this in turn results in VIV at lower windspeeds. The total mass of the tower is approx. 387.73 tons.

The deck stiffness of the vessel is modelled as a rotational spring. In the event that the tower is still on land the foundation is considered infinitely stiff and is modeled as a fixed connection.

Not knowing the structural damping of such a tower, the fundamental damping ratio values are taken from the Eurocode for wind loads. Table 5-1 gives an overview of the tower parameters.

Table 5-1 Tower parameters

Height tower	h	78	[m]
Height, where tapering starts	h_{taper}	52	[m]
Outer diameter top	$D_o\ top$	4	[m]
Outer diameter bottom	$D_o\ bottom$	6	[m]
Thickness	t	0.035	[m]
Steel Density	ρ_{steel}	7800	[kg/m^3]
Youngs modulus	E	$210\text{x}10^6$	[N/m^2]
Mass on top	M_{top}	$9.5\text{x}10^6$	[kg]
Rotational deck stiffness	kr_{deck}	$1.68\text{x}10^{10}$	[Nm/rad]
Structural damping (fundamental mode) *	δ_s	0.012	[-]
Mass of the tower	M_{tower}	$387.73\text{x}10^3$	[kg]

*) As the level of damping is unknown, the Euro code is used as guideline.

5.1.2 Wind conditions

The wind is modeled with a power law. It is assumed that there is a steady wind with no gusts. The maximum windspeed considered here is 38m/s at a reference height of 10m. This corresponds to the survival load case for the installation vessel. A power law coefficient α of 0.09 applies for all the cases studied in this chapter, this value corresponds to the open seas.

5.2 Structural model tower

5.2.1 Sign convention

In the modeling of the tower on the ship the following sign convention is used given by Figure 5-1. In this thesis it is assumed that the ship rotations are around the connection between the deck and the tower. The roll motion is given by Θ_x and the pitch motion is given by Θ_y.

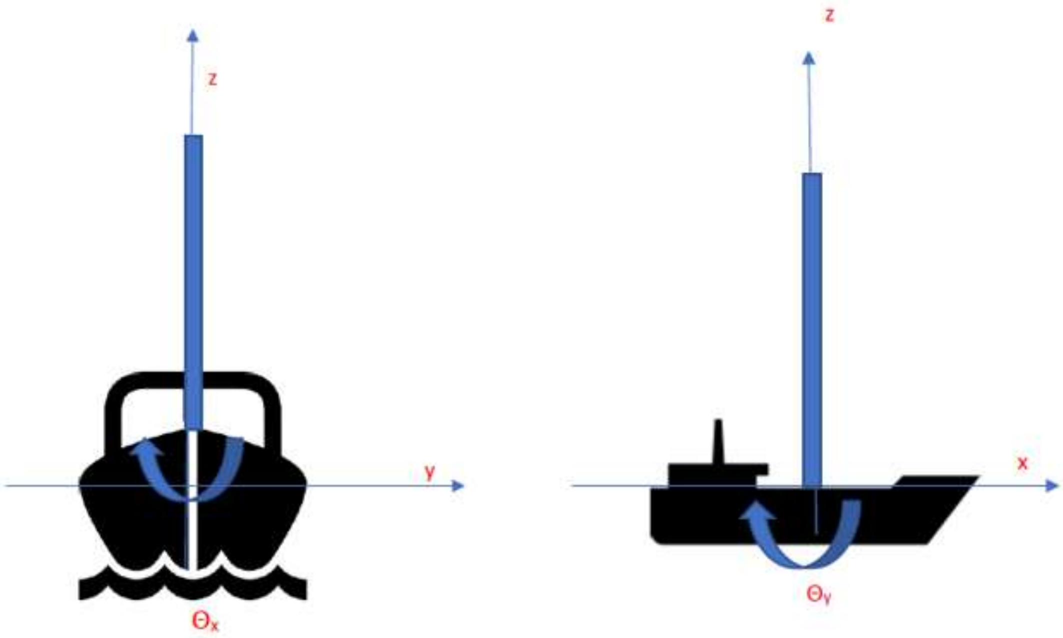

Figure 5-1 Sign convention towers on ship

5.2.2 Boundary and interface conditions

In this chapter different cases with different boundary conditions will be evaluated. At the top the boundary conditions is always the same with a mass on top. On the contrary, at the bottom there are different situation as “Fixed-Fixed” when the tower is in quayside. “Pinned-rotational spring” when the tower is on the ship but no vessel motions are involved. And “Pinned-rotational spring with prescribed motion” if the tower is on the ship with vessel motions included.

Boundary conditions: “Fixed-Fixed”

The Fixed-Fixed boundary conditions are the same as that of the chimney. For brevity it is not written here. They are given by equations (4.4) and (4.5).

Boundary conditions: “Pinned-rotational spring”

This boundary condition is used to model the deck stiffness. In this thesis only the rotational stiffness is taken into account. Here a rotation at the bottom results in a moment proportional to the rotational spring.

- $At\ z = 0$

Crossflow direction:

$$\begin{gathered} Y(0,t) = 0 \\ E^{*}I(0)\frac{\partial^2 Y(z,t)}{\partial z^2}\bigg|_{z=0} = k_{r_Y}\frac{\partial}{\partial z}Y(z,t)\bigg|_{z=0} \end{gathered} \tag{5.1}$$

Inline direction:

$$\begin{gathered} X(0,t) = 0 \\ E^{*}I(0)\frac{\partial^2 X(z,t)}{\partial z^2}\bigg|_{z=0} = k_{r_X}\frac{\partial}{\partial z}X(z,t)\bigg|_{z=0} \end{gathered} \tag{5.2}$$

Boundary conditions: “Pinned-rotational spring with prescribed motion”

This boundary condition is used to model vessel motions with the deck stiffness taken into account. Here it is assumed that the roll and pitch motions are around the base of the tower.

- $At\ z = 0$

Crossflow direction:

$$\begin{gathered} Y(0,t) = 0 \\ E^{*}I(0)\frac{\partial^2 Y(z,t)}{\partial z^2}\bigg|_{z=0} = k_{r_Y}(\frac{\partial}{\partial z}Y(z,t)\bigg|_{z=0} - \theta_X(t)) \end{gathered} \tag{5.3}$$

Inline direction:

$$\begin{gathered} X(0,t) = 0 \\ E^{*}I(0)\frac{\partial^2 X(z,t)}{\partial z^2}\bigg|_{z=0} = k_{r_X}\,(\frac{\partial}{\partial z}X(z,t)\bigg|_{z=0} - \Theta_Y(t))\bigg|_{z=0} \end{gathered} \tag{5.4}$$

Boundary condition: “Mass on top”

This boundary condition is used because the towers have a mass on top of the structure. In this thesis the mass is small and the rotational moment of inertia is neglected so there is no moment on top. There is a shear force however coming from the inertia of the mass. In the continuous form the boundary conditions are written as follows.

- $At\ z = L$

Crossflow direction:

$$E^*I(L)\frac{\partial^2 Y(z,t)}{\partial z^2}\bigg|_{z=L} = 0$$
$$\frac{\partial}{\partial z}(E^*I(L)\frac{\partial^2 Y(z,t)}{\partial z^2})\bigg|_{z=L} + P(L)\frac{\partial Y(z,t)}{\partial z}\bigg|_{z=L} - M_t\frac{\partial Y(z,t)^2}{\partial t^2}\bigg|_{z=L} = 0 \tag{5.5}$$

Inline direction:

$$E^*I(L)\frac{\partial^2 X(z,t)}{\partial z^2}\bigg|_{z=L} = 0$$
$$\frac{\partial}{\partial z}(E^*I(L)\frac{\partial^2 x(z,t)}{\partial z^2})\bigg|_{z=L} + P(L)\frac{\partial X(z,t)}{\partial z}\bigg|_{z=L} - M_t\frac{\partial X(z,t)^2}{\partial t^2}\bigg|_{z=L} = 0 \tag{5.6}$$

Interface conditions:

The tower is modeled as a Euler Bernoulli beam build out of 2 sections. Therefore interface conditions are required. The interface conditions are the same as that of the chimney. For brevity these are not written here. They are given by equations (4.19) and (4.20).

5.2.3 Natural frequencies and mode shapes and damping ratio

Natural frequencies and mode shapes:

Figure 5-2 and Figure 5-3 show the first three mode shapes together with first three undamped natural frequencies. Here the influence of the deck stiffness on the natural frequencies and mode shapes of the tower can be seen. The fundamental natural frequency reduces by almost 40%. Also, the fundamental mode on the vessel looks more like a pendulum.

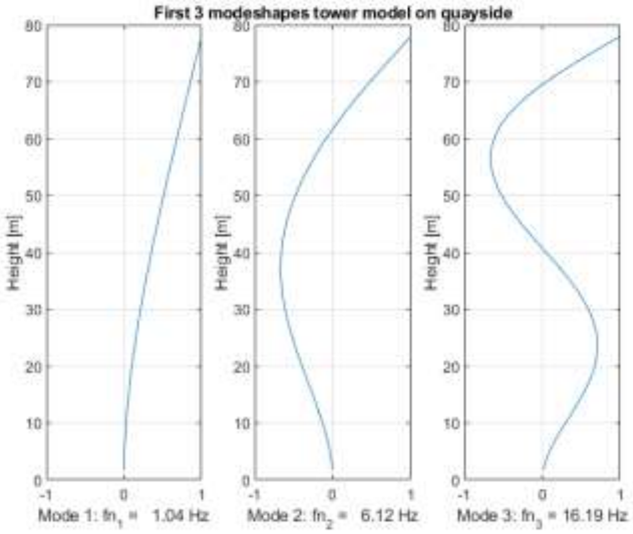

Figure 5-2 First 3 mode shapes on quayside

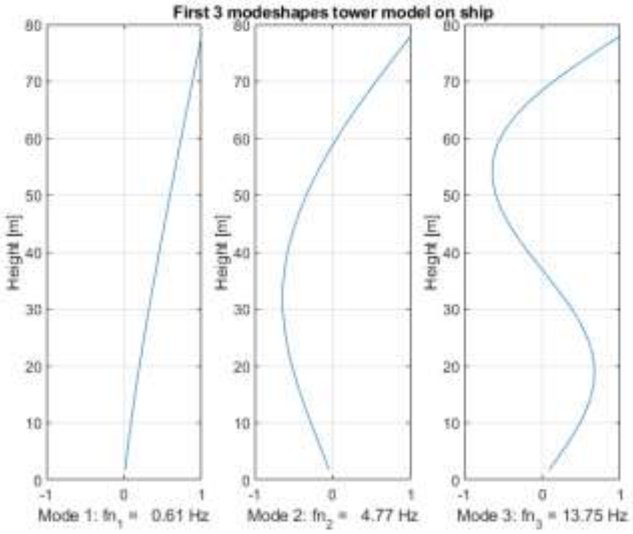

Figure 5-3 First 3 mode shapes on deck

Table 5-2 Eigen frequencies of tower structure

Mode number	Frequency on quayside [Hz]	Frequency on ship [Hz]
1	1.04	0.61
2	6.12	4.77
3	16.19	13.75

Damping ratio:

The damping coefficient, a_1, is set at 0.5833X10^{-3} on quayside and 0.995X10^{-3} on ship. By doing this a logarithmic decrement of damping of 0.012 is achieved in the first mode for both situations. This corresponds to the proposed values of the Eurocode. In the second mode the logarithmic decrement of damping then becomes 0.0703 on quayside and 0.0935 on the ship. In the appendix a detailed explanation is given on determining the logarithmic decrement of damping.

5.3 Case studies

In order to achieve the sub research objectives four different cases are studied. A short description of each case is given below.

Case A: Towers on quayside:

The first case represents the towers are still on quayside. Because of the stiff foundation it is expected that VIV will occur only at higher windspeeds.

Case B: Towers on ship jacked:

This case represents the tower on the ship but not sailing. Here due to the lower natural frequencies it is expected that the VIV will occur much earlier.

Case C: Towers on ship with roll motion:

In the third case the ship is sailing so here we have a combined loading from the ship motion and the VIV. It is assumed that the waves are coming from the same direction as the wind. This means that the ship motions move the tower in the inline direction.

Further only the roll motion is considered, because the roll motion results in the largest displacements. The roll motion is modeled as a simple sine with a roll period of 10 seconds and a roll amplitude of 8 degrees. See equation (5.7) and Figure 5-4.

$$\Theta_x(t) = A_{roll}\sin(\frac{1}{T_{roll}} * t) \qquad (5.7)$$

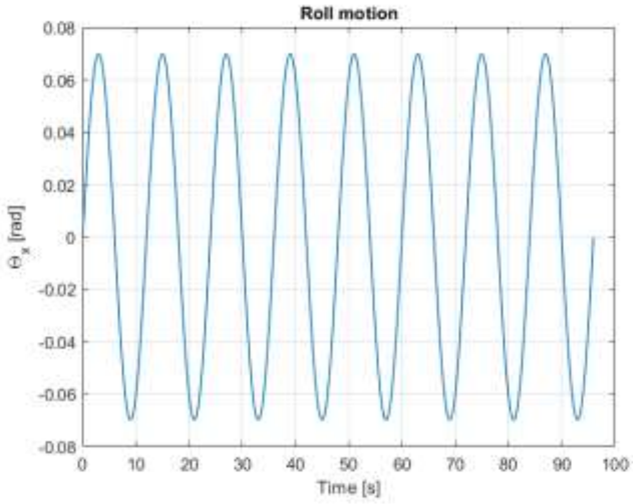

Figure 5-4 Roll motion Case C

Due to the roll motion there is a moment acting on the deck of the ship. Figure 5-5 (a) shows the bending moment for 1000 seconds of simulation time. It can be seen that the bending moment in the beginning of the simulation is larger, this comes due to the inertia of the tower. But after approximately 400 seconds a steady state is found. Figure 5-5 (b) zooms in on the last 100 seconds of the simulation. In the steady state the bending moments coming from the roll motions are around 7x10^7Nm. It is obvious that there is more than one frequency in the steady state bending moment.

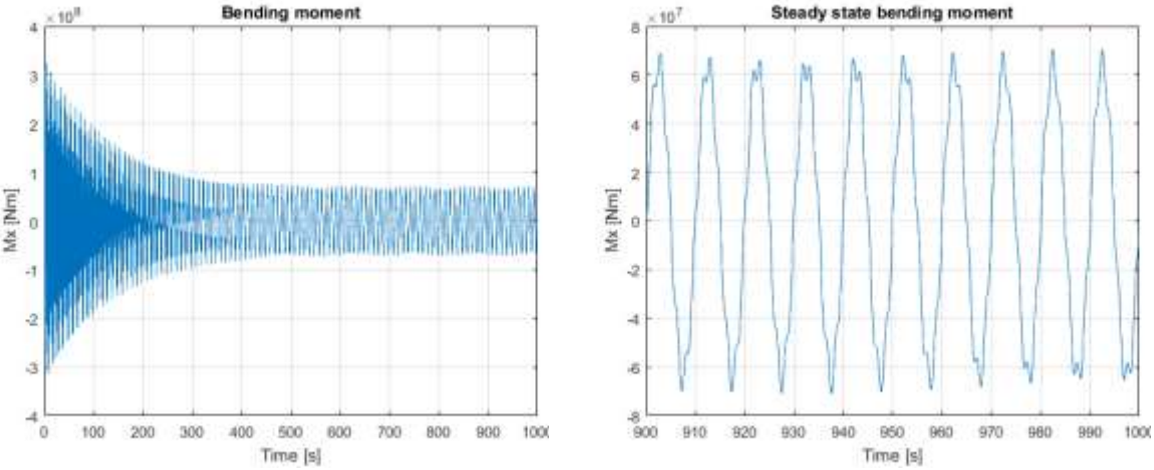

(a) (b)

Figure 5-5 Bending moment at deck coming from roll motion

Figure 5-6 gives the power spectral density of the bending moment in the steady state. We can see that most energy is at 0.1 Hz which is exactly the roll natural period. This is because the structure is excited at this frequency. Further there is also some energy in the fundamental natural frequency.

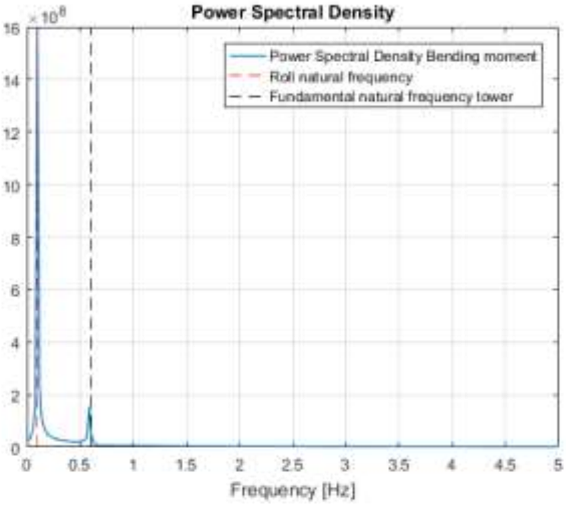

Figure 5-6 Power Spectral Density of the bending moment due to roll

Case D: Towers with strakes

In this case the top one third of the tower is covered by strakes. From literature (Zdravkovich, 1981) it is found that only the top one third of the tower needs to be covered if only the fundamental mode is excited. Zdravkovich also states that the drag for strakes is approximately twice the normal values. This increase in drag will increase the in-line force and is called the drag penalty. In the modelling of the strakes it is assumed that there is no lift force at al at that part.

Simulation

For the simulations the same procedure as the chimney is followed. Where winds speeds from 1 m/s with increasing steps of 1m/s up till a maximum windspeed of 38 m/s at a reference height of 10m are simulated. At every windspeed the simulation is run for 1000s of simulation time. This was enough to reach the steady state of vibration. At this point the steady state amplitude is measured. The maximum bending moment and shear forces are also calculated at each wind speed. After which the windspeed is increased. At the "next windspeed" the steady state amplitude measurement again and this is repeated until 38m/s is reached.

The tuning parameters, A and ϵ are chosen respectively as 16 and 0.4. For the stationary drag and lift force coefficients first the values of the supercritical regime are used and are given as follows, $C_{LO} = 0.1$ and $C_{DO} = 0.8$. At the parts where the tower is covered with strakes these values become $C_{LO} = 0$ and $C_{DO} = 1.6$. Table 5-3 gives a complete overview of the input parameters for each case with super critical force coefficients.

Table 5-3 Simulation input case study: super critical force coefficients

		Case A	Case B	Case C	Case D		
Coupling parameter	A	16	16	16	16		[-]
Tuning parameter	ϵ	0.4	0.4	0.4	0.4		[-]
Stationary lift force coefficient	C_{LO}	0.1	0.1	0.1	0.1	0	[-]
Stationary drag force coefficient	C_{DO}	0.8	0.8	0.8	0.8	1.6	[-]
Strouhal number	St	0.198	0.198	0.198	0.198		[-]
Windspeed at 10 m	v_{10}	1-38	1-38	1-38	1-38		[m/s]
Wind power law coefficient	α	0.09	0.09	0.09	0.09		[-]
Roll period	T_{roll}	-	-	10	-		[s]
Roll amplitude	A_{roll}	-	-	8	-		[°]
Pitch period	T_{pitch}	-	-	-	-		[s]
Pitch amplitude	A_{pitch}	-	-	-	-		[°]

A second set of simulations is done where were we neglect the Reynolds number dependency and assume the force coefficients as they are in the sub critical flow regime with $C_{LO} = 0.315$ and $C_{DO} = 1.2$. At the parts where the tower is covered with strakes these values become $C_{LO} = 0$ and $C_{DO} = 2.4$. Table 5-4 gives a complete overview of the input parameters for each case with sub critical force coefficients.

Table 5-4 Simulation input case study: sub critical force coefficients

		Case A	Case B	Case C	Case D		
Coupling parameter	A	16	16	16	16		[-]
Tuning parameter	ϵ	0.4	0.4	0.4	0.4		[-]
Stationary lift force coefficient	C_{LO}	0.315	0.315	0.315	0.315	0	[-]
Stationary drag force coefficient	C_{DO}	1.2	1.2	1.2	1.2	2.4	[-]
Strouhal number	St	0.198	0.198	0.198	0.198		[-]
Windspeed at 10 m	v_{10}	1-38	1-38	1-38	1-38		[m/s]
Wind power law coefficient	α	0.09	0.09	0.09	0.09		[-]
Roll period	T_{roll}	-	-	10	-		[s]
Roll amplitude	A_{roll}	-	-	8	-		[°]
Pitch period	T_{pitch}	-	-	-	-		[s]
Pitch amplitude	A_{pitch}	-	-	-	-		[°]

Results from the super critical force coefficients:

Figure 5-7 (a) shows the cross-flow displacements at the tip of the tower of each case against the windspeed at 10m height. With a cross-flow vibration amplitude of approximately 0.025 diameters the largest displacements are found at 28 m/s for case A. Case B and C both have approximately a cross-flow vibration amplitude of 0.021 diameters at 16 m/s. This means that the ship motions do not seem to influence the crossflow displacements. Further it can be seen that for case D the cross-flow vibration amplitude is only 0.007 diameters at 16 m/s.

The in-line displacements at the tip against the windspeed are shown in Figure 5-7 (b). Notice that for all the cases the largest values are at the highest windspeed of 38 m/s. With 0.007 diameters case A has the smallest in-line displacement. This is due to the high stiffness, larger forces are required for the same displacement. In case B the in-line displacement is 0.019. This is larger than case A since this is a less stiff structure. Case C the in-line displacement is the largest of all cases. The maximum value here is 0.103 diameters. This comes due to the roll motion of the vessel. With 0.03 diameters in-line displacement, case D has a larger in-line displacement then case B. This is due to the effect of the increased drag.

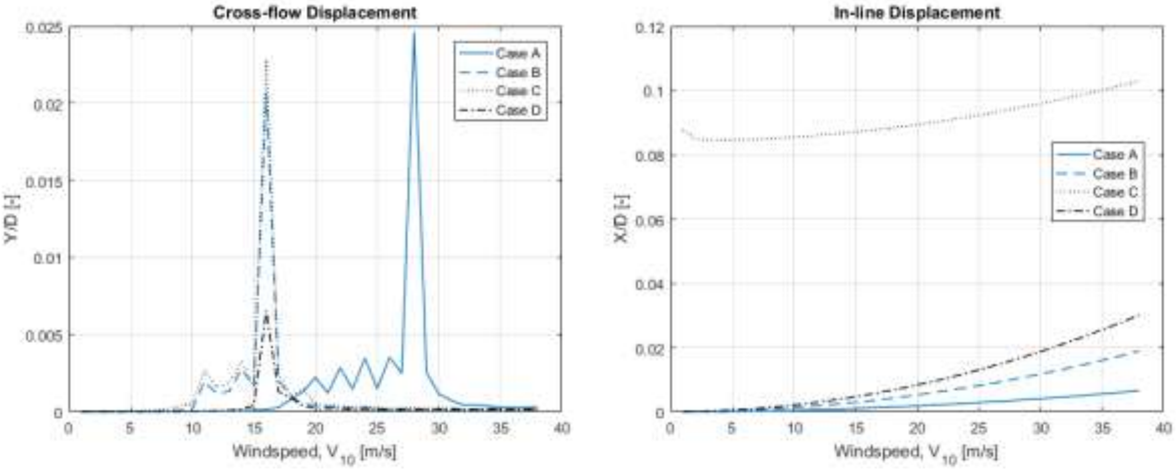

(a) (b)

Figure 5-7 Displacements with force coefficients from the super critical regime

Another interesting result to look at is the bending moments at the deck of the ship. Figure 5-8 (a) gives the cross-flow bending moments (over the x-axis). With 5.22x10^7Nm, case A has the largest cross-flow bending moment at 28 m/s. Note that this is in the order of magnitude of the bending moments coming from the ship motion. Further, for case B and C the bending moment is approximately 1.75x10^7Nm at 16m/s. So, in the cross-flow motion the bending moment is not influenced by the sip motion. Finally, case D has the smallest cross-flow bending moment of 5.32x10^6Nm at 16 m/s, which is approximately 70 % smaller than case B and C. So, the strakes seem to be an effective measure.

Figure 5-8 (b) shows the in-line bending moments (over the y-axis) for the different cases. Just as in the in-line displacement the maximum values for the in-line bending moments are found at the highest windspeed. It is interesting to see that for case A and case B the in-line bending moments are the same with 1.59x10^7Nm. this can be explained by the fact that the in-line forces are mainly coming from the drag part of the forcing. And since the drag is exactly the same in these two cases, the bending moments are the same. With 8.04x10^7 Nm, case C has by far the largest in-line bending moment, this comes by the fact that the ship motions have a large contribution. Further with 2.47x10^7Nm for case D the in-line bending moment increased by 55% compared to case A and B. This increase comes from the increased drag from the strakes.

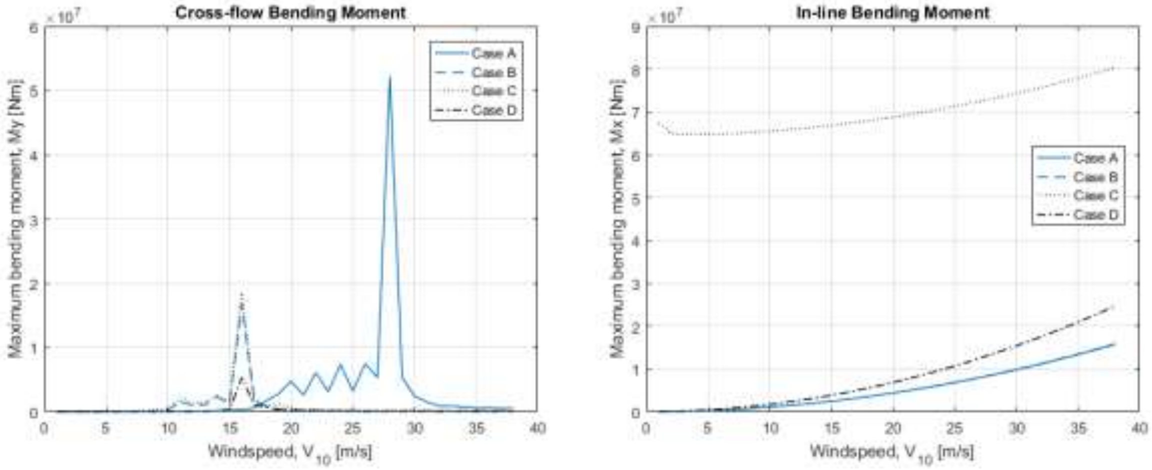

(a) (b)

Figure 5-8 Bending moments at deck with force coefficients from the super critical regime

Results with sub critical force coefficients:

Figure 5-9(a) gives the cross-flow displacements at the tip of each case against the windspeed at 10m height with the sub critical force coefficients. Case A and B both have a cross-flow vibration amplitude of approximately 0.29 diameters. The largest displacements are found at 29 m/s for case A and at 17m/s for case B. With 0.3 diameters at 17 m/s case C has a slightly higher cross-flow vibration amplitude. This means that the ship motion slightly increases the cross-flow vibration amplitude. The effect of the strakes can be seen in case D, the cross-flow vibration amplitude is only 0.05 diameters at 17 m/s. This is a decrease of 80 % in cross-flow vibration amplitude compared to no strakes.

The in-line displacements at the tip against the windspeed are shown in Figure 5-9 (b). Notice that for all the cases the largest values are at the highest windspeed of 38 m/s. Again, due to the high stiffness case A has the smallest in-line displacement of 0.009 diameters. In case B the in-line displacement is 0.028 diameters. Due to the roll motion of the vessel, case C has the largest in-line displacement of all cases. The maximum value here is 0.11 diameters. Finally, with 0.045 diameters in-line displacement, case D has a larger in-line displacement then case B. This is due to the effect of the increased drag.

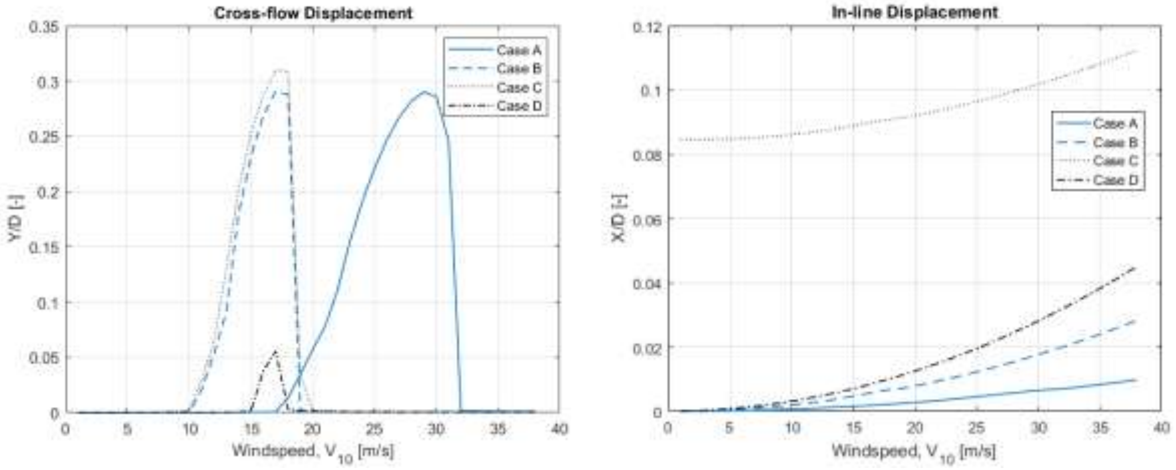

(a) (b)

Figure 5-9 Displacements with force coefficients from the sub critical regime

Figure 5-10 (a) gives the crossflow bending moments. For case A the cross-flow bending moments are the largest. This can be explained by the larger natural frequency. The frequency of vibration follows the natural frequency. And a higher frequency of vibration means larger accelerations. Larger accelerations result in higher loads.

Case D has the smallest cross-flow bending moment. This proof the effectiveness of the strakes. Further, the cross-flow bending moments from case B and C are almost the same. This means that the ship motions have no significant influence on the cross-flow loads.

The in-line bending moments are found in Figure 5-10 (b). Here case A and B have approximately the same values. This is because in these cases the in-line bending moment comes mainly from the drag. And since the drag is the same in these two cases the in-line bending moment is also the same. Also notice that the effect of the extra drag coming from the strakes we see in the bending moment of case D. This is slightly higher than case A and B.

The largest in-line bending moments can be found for case C. This is a result from the large contribution of the bending moment coming from the roll motion.

It is interesting to note that the cross-flow bending moments here are much larger than the bending moments coming from the roll motion. This means that VIV are the dominating loads.

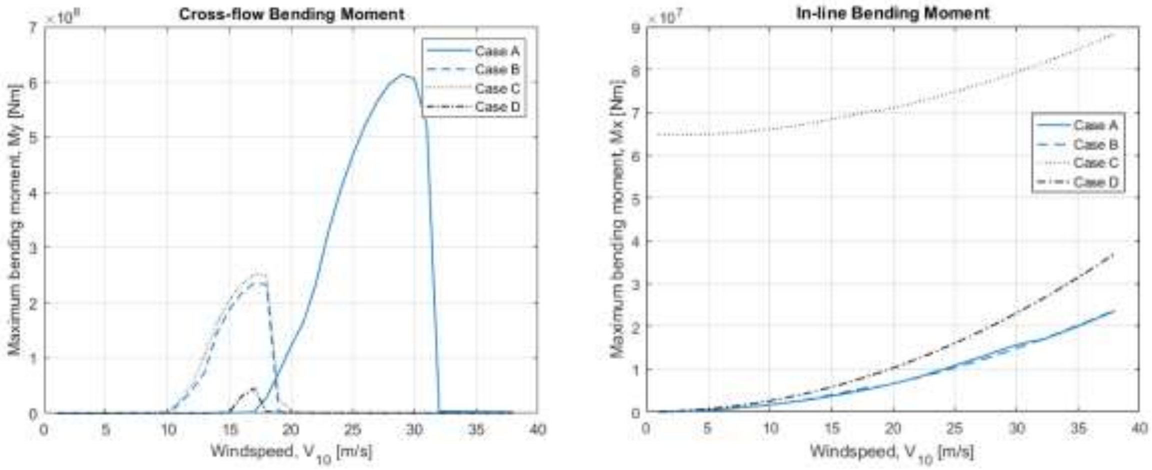

(a) (b)

Figure 5-10 Bending moments with force coefficients from the sub critical regime

Reduced velocities

It is also interesting to look at the reduced velocities at the largest vibration amplitudes. Figure 5-11 (a) shows the reduced velocity at a windspeed of 16 m/s. Figure 5-11 (b) shows the reduced velocity at a windspeed of 28m/s. In the graphs the dotted lines are the reduced velocities for the cases on the ship. And the solid line is the reduced velocity at quayside.

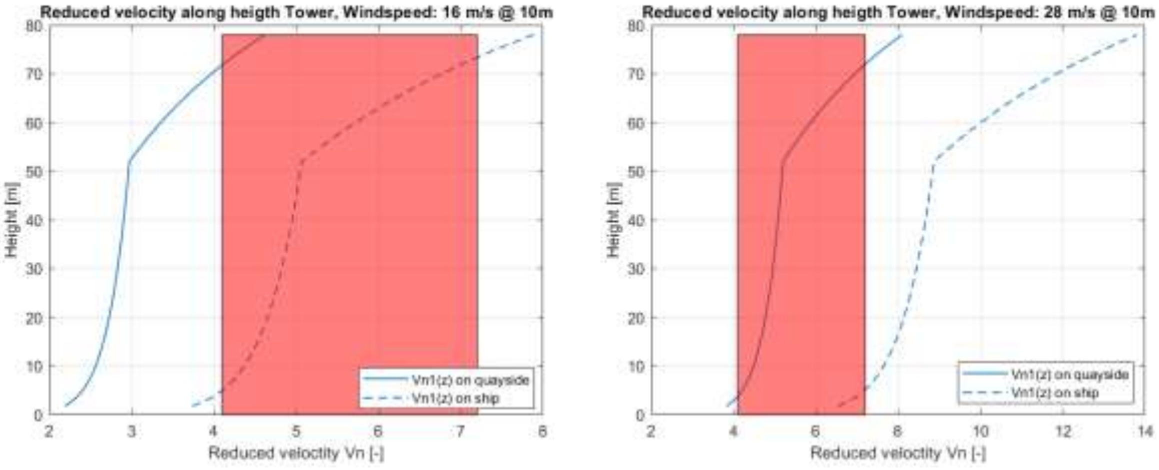

(a) (b)

Figure 5-11 Reduced velocities at the largest vibration amplitudes

At 16m/s large parts of the reduced velocity for the cases on the ship are at the values where we would expect VIV for a rigid cylinder. At a windspeed of 28 m/s the reduced velocity for the tower on quayside is within the lock-in range. An interesting observation is that for both situation the top part is not at the reduced velocity where we would expect VIV for a rigid cylinder. This would suggest that at the top of the tower energy is dissipated.

5.4 Conclusions

Based on the case study better understanding is gained. With this understanding the following conclusions are drawn.

- For the tower studied in this thesis only the fundamental mode in excited. The towers are too stiff to excite the second mode in the wind conditions that are expected.
- A lower deck stiffness will result in VIV earlier, but an lower deck stiffness also results in lower loads.
- The ship motions seem to have no influence on the VIV. This can be explained by the fact that the frequency of the ship motion is too far away from the vibration frequency of the VIV for them to interact.
- Strakes as mitigation is proven technology, in the model it is shown that covering only 1/3 of the structure with strakes reduces the VIV significantly. There is indeed a drag penalty however this is not so large!
- When the super critical force coefficients are used, VIV is much less severe. The lock-in range is smaller and the maximum bending moments are then in the order of the bending moments coming from ship motions.
- When the sub critical force coefficients are used, VIV is very severe. The lock-in rage is bigger and the bending moments from the VIV are larger by an order of 10 times than the bending moments coming from ship motions.
- Even though different vortex shedding frequencies are across the height of the tower, the tower always seems to be vibrating at its natural frequency.
- At the largest vibration amplitudes, the top part is not in the reduced velocities where VIV would occur for rigid cylinders.

6 Conclusion and recommendations

This chapter gives an short summary then the conclusion and finally some recommendations are given.

In this thesis the main objective was to explore the possibility of modelling the VIV of flexible cylindrical structures. This was achieved by first the modeling of VIV of an rigid cylinder. Next the model was extended to the modelling of flexible structures. To see how well the model performs against real VIV, an attempt was made to model the VIV of an in situ chimney. Finally the modeling of a sea fastened wind turbine towers was done. Here a case study gave answers to the sub objectives.

6.1 Conclusions

6.1.1 VIV modeling of an rigid cylinder with high mass damping ratio (Feng)

- The tuning parameters found in earlier research for low mass damping ratio experiments fail to predict the lower branch and upper branch.
- For increasing windspeed the wake-oscillator model can predict the lower branch of Feng's experiment good by making use of the right tuning parameters. For decreasing wind speed a discrepancy was found.

6.1.2 VIV modeling of an in situ chimney

- The chimney studied in this thesis was in the super critical flow regime, here we would expect a Strouhal number of 0.4 for smooth stationairy cylinders. But the measured Strouhal number was 0.21. This would suggest that the chimney is in the sub critical flow regime. This discrepancy can have two possible explanations. The chimney was not that smooth. Or the Strouhal number is different for flexible cylinders.
- Totally neglecting the Reynolds number dependency result in an overestimation of the cross-flow vibration amplitude.
- Due to the sheared wind there are different frequencies over the height of the chimney, but the frequency of vibration is always at its natural frequency.

6.1.3 VIV modeling of sea fastened wind turbine tower

- Ship motions have no influence on the VIV. The frequencies are too far apart from each other to interact.
- Only covering the top third part of the tower with strakes seem to reduced significant.
- The deck stiffness is an important parameter for the natural frequency of the system. Increasing the deck stiffness will result in VIV at a higher windspeed. But this will also increase the loads on deck.
- In this case study only the fundamental mode is excited in wind conditions until the survival load case. But with increasing tower heights it is likely that the towers will become less stiff and then maybe the second mode can also be excited.

6.2 Recommendations

- Wind induced vibration is a very complex phenomenon, with a lot of dependencies such as Reynolds, Surface roughness, turbulence of incoming wind flow etc. The wake oscillator model makes a lot of simplifications. Therefore, it is advised to perform full scale measurements to gain better understanding.
  With the following equipment:
    - Pressures sensors for the wind loads acting on tower
    - Accelerometers in the tip of the tower. Since only the first mode is excited the maximum displacements are expected to be here.
    - Strain gauges can be placed along the tower/deck, this way we can measure the bending moments along the tower.
    - Anemometers, to measure wind speeds.
- In this thesis only one tower is considered on the ship. But in reality multiple towers are being transported at once. For this it is recommended to do an CFD analysis or wind tunnel testing for better understanding on how towers influence each other.
- Damping is also an important parameter for the VIV. For a more accurate model the real-life modal damping values are required. This might be obtained from measurements. (Free vibrations)
- Increasing tower sizes will make the towers more flexible lowering the natural frequencies. This in turn results in VIV at lower windspeeds and maybe even VIV in the second mode. The more flexible towers are also a problem during installation, because there are larger vibration amplitudes. So, advised to do more research into an integrated vibration mitigation system that can be used during transport and during installation.

Bibliography

Blevins, R. D. (1990). *Flow-Induced Vibration* (second ed.). New York: Van Nostrand Reinhold.

Facchinetti, M. L., de Langre, E., & Biolley, F. (2004). Coupling of structure and wake oscillators in vortex-induced vibrations. *Journal of Fluids and Structures, 19*, 123-140.

Feng, C. C. (1968). *The Measurement of Vortex Induced Effects in Flow Past Stationary and Oscillating Circular and D-section Cylinders.* M.Sc. Thesis, The University of British Colombia.

Gabbai, R. D., & Benaroya, H. (2005). An overview of modeling and experiments of vortex-induced vibration of circular cylinders. *Journal of Sound and Vibration, 282*, 575-616.

Galemann, T., & Ruscheweyh, H. (1992). Measurements of wind induced vibrations of a fullscale steel chimney. *Journal of Wind Engineering and Industrial Aerodynamics, 41*, 241-252.

Ogink, R. H., & Metrikine, A. V. (2010). A wake oscillator with frequency dependent coupling for the modeling of vortex-induced vibration. *Journal of Sound and Vibration, 329*, 5452-5473.

Rao, S. S. (2004). *Mechanical Vibrations.* New Jersey: Pearson Education, Inc.

Ruscheweyh, H., & Galemann, T. (1996). Full-scale measurements of wind-induced oscillations of chimneys. *Journal of Wind Engineering and Industrial Aerodynamics, 65*, 55-62.

Sumer, B. M., & Fredsøe, J. (1997). *Hydrodynamics Around Cylindrical Structures.* Singapore: World Scientific Publishing.

Zdravkovich. (1981). Review and classification of various aerodynamic and hydrodynamicmeans for suppressing. *Journal ofWind Engineering and Industrial Aerodynamics, 7*, 145-189.

Appendix A Feng Simulations

The full simulation results of chapter 3 with the tuning parameters $A = 16$ and $\epsilon = 0.4$ are given in Figure A-1.

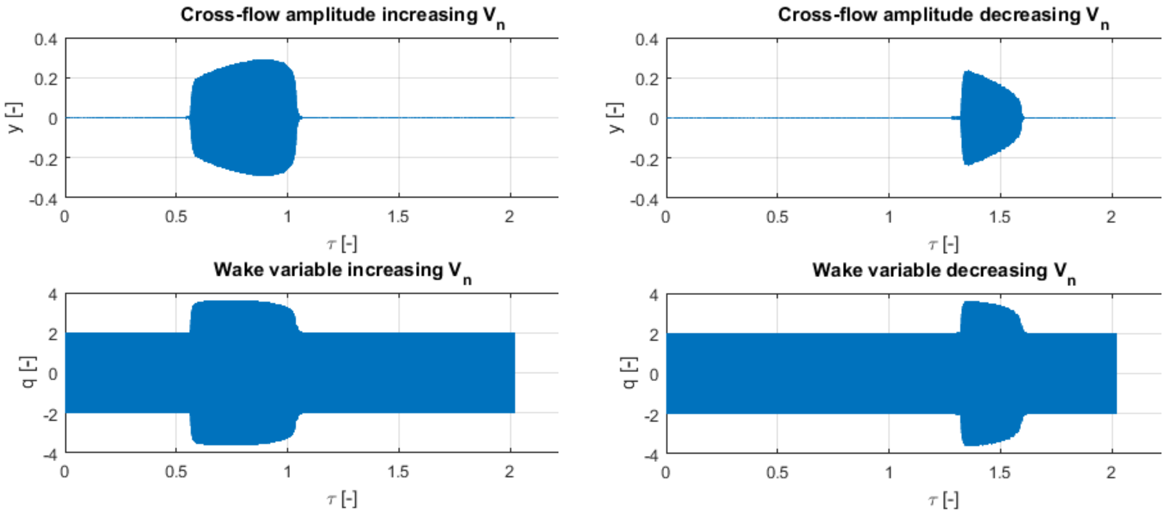

(a) (b)

Figure A-1 Simulation results increasing and decreasing Vn. Tuning Parameters: A = 16 and ϵ = 0.4

An interesting observation from the simulation is that the wake variable is amplified in the lock-in range. And outside the lock-in range the wake-variable oscillates within its limit cycle of 2. This is the same as it was seen before for the forced Van der Pol oscillator.

Appendix B Programming Flow Chart

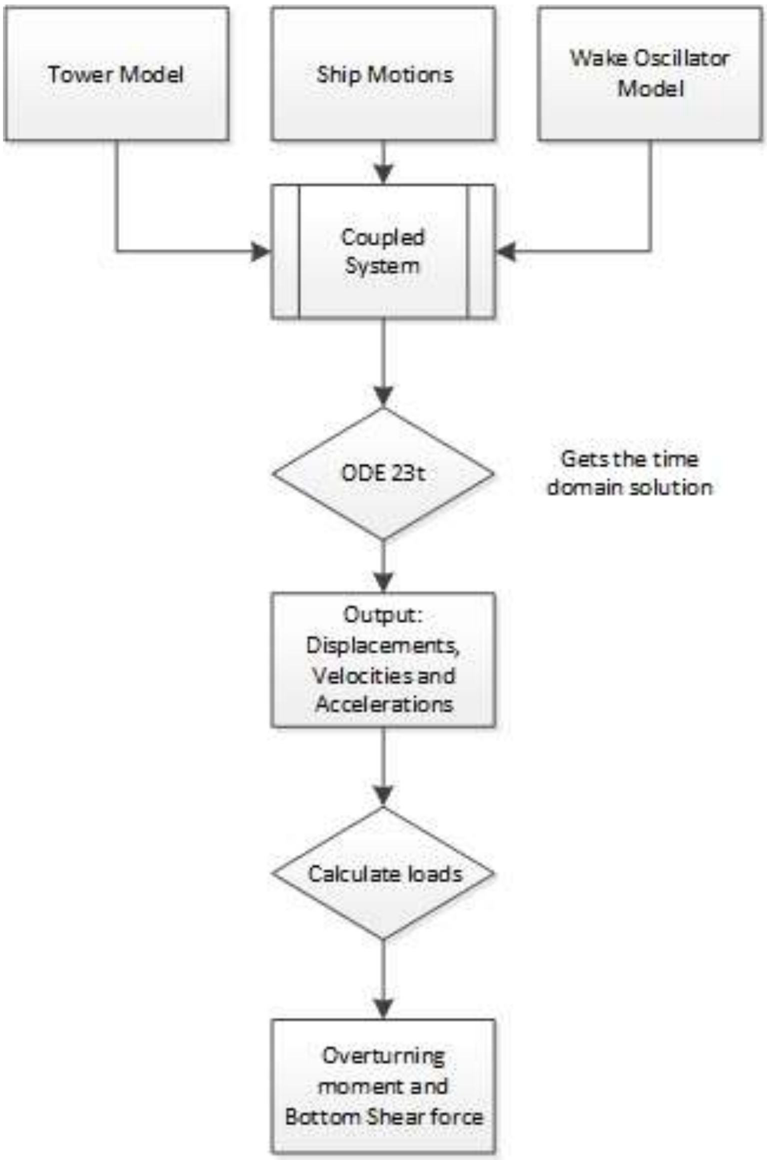

Figure B-1 Programming flow chart

Appendix C Natural frequencies/Mode shapes/Damping ratios

Natural frequencies and Mode shapes

It is possible to write the discretized equations of motion in the familiar matrix notation. The undamped natural frequencies and mode shapes are then obtained by solving the eigenvalue problem.

$$|-\omega^2 \boldsymbol{M} + \boldsymbol{K}| = 0$$

Here the natural frequencies are found by taking the square root of the eigenvalues and the mode shapes are the eigenvectors.

Damping ratio

Determining the damping ratio from the logarithmic decrement:

By the way we implanted damping to our system we don't know in advance what modal damping ratio belongs to the first mode. By giving the beam an initial displacement in the first mode shape it will vibrate in this mode and eventually damp out. This ´free vibration experiment´ can be solved by the ODE 23t solver from MATLAB.

From the simulatio results, the modal damping ratio can then be determined from the logarithmic decrement. The logarithmic decrement represents the rate at which the amplitude decreases of a free-damped vibration. (Rao, 2004)Given by the equation below.

$$\delta = \frac{1}{m} \ln(\frac{y_1}{y_{m+1}})$$

Where, δ is the logarithmic decrement
m is the number of amplitudes further
y is the amplitude

Approximate values of the logarithmic decrement of structural damping are given by the Eurocode. For unlined welded steel stacks, the value is $\delta_s = 0.012$ in the fundamental mode. This corresponds to a damping ratio of $\zeta_s = 0.0019$.

From the logarithmic decrement the damping ratio can then be found by the equation below

$$\zeta = \frac{\delta}{\sqrt{(2\pi)^2 + \delta^2}}$$

All that is left to do is to find the right value from the material damping parameter, α. This requires some tuning; the desired damping levels can be found by this method.

Moment and Shear force relations

If the displacements are known the moment and shear force can be calculated by the relations known from the Euler Bernoulli beam theory.

The moment relations are:

$$M_x(z) = EI(z)\frac{\partial^2 x}{\partial z^2}$$

$$M_y(z) = EI(z)\frac{\partial^2 y}{\partial z^2}$$

The shear force relations are:

$$V_x(z) = \frac{\partial}{\partial z}\left(EI(z)\frac{\partial^2 x}{\partial z^2}\right)$$

$$V_y(z) = \frac{\partial}{\partial z}\left(EI(z)\frac{\partial^2 y}{\partial z^2}\right)$$

List of Figures

List of Tables